



**HAL**  
open science

## Synsedimentary to early diagenetic rejuvenation of barite-sulfides ore deposits: Example of the Triassic intrakarstic mineralization in the Lodève basin (France)

D. Laurent, M. Lopez, P.-J. Combes, C. Guerrot, J.E. Spangenberg, E.C. Gaucher

### ► To cite this version:

D. Laurent, M. Lopez, P.-J. Combes, C. Guerrot, J.E. Spangenberg, et al.. Synsedimentary to early diagenetic rejuvenation of barite-sulfides ore deposits: Example of the Triassic intrakarstic mineralization in the Lodève basin (France). *Marine and Petroleum Geology*, 2020, 119, pp.104464. 10.1016/j.marpetgeo.2020.104464 . hal-02912521

**HAL Id: hal-02912521**

**<https://hal.umontpellier.fr/hal-02912521>**

Submitted on 22 Aug 2022

**HAL** is a multi-disciplinary open access archive for the deposit and dissemination of scientific research documents, whether they are published or not. The documents may come from teaching and research institutions in France or abroad, or from public or private research centers.

L'archive ouverte pluridisciplinaire **HAL**, est destinée au dépôt et à la diffusion de documents scientifiques de niveau recherche, publiés ou non, émanant des établissements d'enseignement et de recherche français ou étrangers, des laboratoires publics ou privés.



Distributed under a Creative Commons Attribution - NonCommercial 4.0 International License

1        **Synsedimentary to early diagenetic rejuvenation of barite-sulfides ore deposits:**  
2        **Example of the Triassic intrakarstic mineralization in the Lodève basin (France)**

3  
4        D. Laurent<sup>a\*</sup>, M. Lopez<sup>a</sup>, P-J. Combes<sup>a</sup>, C. Guerrot<sup>b</sup>, J.E. Spangenberg<sup>c</sup>, E. C. Gaucher<sup>d</sup>

5  
6        <sup>a</sup> Geosciences Montpellier, University of Montpellier, 34090 Montpellier, France

7        <sup>b</sup> BRGM/LAB, 45060 Orléans, France

8        <sup>c</sup> Institute of Earth Surface Dynamics (IDYST), University of Lausanne, Lausanne,  
9        Switzerland

10       <sup>d</sup> TOTAL-Scientific and Technical Center Jean Féger (CSTJF) – TOTAL, 64000 Pau, France

11  
12  
13       **\*Corresponding author:** Dimitri Laurent, present-day address: 20 rue du faubourg des trois  
14       maisons, 54000 Nancy, France.

15       E-mail address: [dimit.laurent@gmail.com](mailto:dimit.laurent@gmail.com)

16       Phone: +33 (0) 6 83 89 41 82.

17  
18       **Number of words of text (without abstract, bibliography and figure captions): 8632**

19       **Number of references: 89**

20       **Number of figures: 15**

21       **Number of tables: 2**

22       **Number of appendices: 1**

23       **Abbreviated title:** Synsedimentary to early diagenetic rejuvenation of barite-sulfides ore de-  
24       posits

25 **Abstract**

26         The exhumed Lodève Basin (Hérault, France) provides a rich suite of outcrops  
27 showing diagenetic Ba-Pb-Fe-Cu fronts trapped in karst system in Cambrian dolomites during  
28 the Triassic post-rift exhumation of the basin. The sedimentological analysis on 10 sites in the  
29 basin reveals that barites-sulfides fronts formed during humid-arid climate fluctuations and  
30 the emplacement of a shallow lake environment. The fabric of ore deposits, the  
31 microthermometry of fluid inclusions entrapped within barites and the strontium/sulfur  
32 isotopic compositions of barite-sulfides associations reveal two distinct groups of  
33 mineralizations, Type I and Type II, which are contemporaneous but resulting from different  
34 processes. The synsedimentary mineralization of the Type I, the presence of only primary  
35 single-phase liquid fluid inclusions within barite crystals and the gradual increase of  $\delta^{34}\text{S}$  for  
36 both barites and chalcopyrites with depth (from -7 to +18.9‰ V-CDT) suggest ore  
37 precipitation close to the vadose zone under bacterial sulfate reduction (BSR) in a confined  
38 sulfate-rich playa lake aquifer. The similar  $^{87}\text{Sr}/^{86}\text{Sr}$  ratios between barites and the overlying  
39 Triassic evaporites indicate that the barium and strontium derived directly from the overlying  
40 sulfate-rich lake. For the Type II, the high homogenization temperature of fluid inclusion  
41 entrapped within barite (modal Th between 60 and 80°C) and the association with  
42 hydrocarbon markers, confirm the participation of deeper basinal brines in addition to  
43 downward percolating sulfate derived from the lake environment. The high positive values of  
44  $\delta^{34}\text{S}$  for both barites and sulfides are typical of a precipitation linked to the combined action  
45 between anaerobic oxidation of methane and sulfate reduction (AOM-SR) at the sulfate-  
46 methane transition zone (SMTZ) during hydrocarbon migration. Similar  $^{87}\text{Sr}/^{86}\text{Sr}$  ratios  
47 between Middle Triassic barites and previous Late Permian barites confirm that the source of  
48 metals precipitated at the SMTZ originated from the dissolution of anterior ore deposits  
49 located in the sulfate-depleted zone. This study links very shallow metallogenesis processes to  
50 reworking of MVT ore deposits by the action of sulfate-reducing bacteria around hydrocarbon  
51 seeps in a karstic environment.

52

53 **Keywords:** *karst; ore deposit; diagenetic barite; playa lake; sulfate reduction; fluid*  
54 *inclusions; sulfur and strontium isotopes.*

## 55 1. Introduction

56 A metallogenic cycle in a sedimentary basin can be summarized by four main key  
57 elements (Routhier, 1980): source, transport, deposition and remobilization of metals. If the  
58 three first steps are already well understood, the mechanism of remobilization needs to be  
59 better constrained. In particular, several questions remain concerning the nature of factors that  
60 control the redistribution of metals and its timing during the basin structuring (extension,  
61 compression, tectonic quiescence, etc...). If structural and stratigraphic controls are  
62 predominant in the formation of sulfur-rich sediment-hosted deposits such as Mississippi  
63 Valley-Type (MVT) or SEDimentary EXhalative (SEDEX) and often linked to the mature  
64 burial stage of sedimentary basin (topography-driven, sediment compaction, orogenic  
65 squeezing, overpressured reservoirs, thermal and density reflux drives; Leach et al., 2010), the  
66 rejuvenation of these ore deposits can occur during early diagenesis. In particular, barium-  
67 sulfides mineralization are known to form close to the sediment-water interface (SWI) due to  
68 metal remobilization (e.g. Torres et al., 1996; Riedinger et al., 2006). The cycle of barium is  
69 part of the debate about early diagenetic ore deposits rejuvenation, particularly linked to the  
70 formation of shallow diagenetic fronts related to the sulfate-methane transition zone (SMTZ)  
71 few meters under the SWI (e.g. Goldberg and Arrhenius, 1958; Brumsack, 1986; Torres et al.,  
72 1996). The SMTZ consists in a chemical boundary at the meeting place between downward  
73 diffusing sulfates coming from the overlying seawater and the upward circulating  
74 biogenic/thermogenic methane originated from deeper sources. This diagenetic transition  
75 results from a coeval activity of sulfate-reducing bacteria (bacterial sulfate reduction – BSR;  
76 Machel et al., 1995; Machel, 2001) and the methane-oxidizing Archaea (Anaerobic Oxidation  
77 of Methane – AOM; Reeburgh, 1976; Reeburgh, 1983) that consumes dissolved sulfates.  
78 Therefore, the SMTZ limits an underlying sulfate-depleted zone where primary barites are



79 dissolved (Barnes and Goldberg, 1976; Reeburgh, 1976; Borowski et al., 1999; Aloisi et al.,  
80 2004; Rodriguez et al., 2000; Dickens, 2001; Niemann et al., 2006). The barium ions released  
81 into the porewater then diffuse upward or can be moved with sedimentary brines along  
82 permeable pathways (Kastner et al., 1990) up to a zone just above the SMTZ where  $\text{SO}_4^{2-}$  is  
83 available, and precipitate to form authigenic barite-sulfides fronts (e.g. Torres et al., 1996;  
84 Br  h  ret and Brumsack, 2000; Aloisi et al., 2004; Arndt et al., 2006; Riedinger et al., 2006).  
85 However, the role of SMTZ in the remobilization and precipitation of diagenetic barite-sulfide  
86 fronts is only demonstrated in marine environment away from terrestrial influence, while  
87 some continental depositional environments, such as playa lake, can led to similar chemistry  
88 conditions. In addition, the major part of studies on SMTZ are mostly based on offshore 1D  
89 core data (Torres et al., 1996; Aquilina et al., 1997; Riedinger et al., 2006; Snyder et al., 2007;  
90 Borowski et al., 2013; Arning et al., 2015; Magnall et al., 2016; Hu et al., 2017) as very few  
91 outcrop analogues have been evidenced that can give a 3D view of such shallow  
92 metallogenesis (Zhou et al., 2015; Fernandes et al., 2017).

93 The continental Lod  ve basin contains several Ba-F-Cu-Pb-Fe ore deposits infilling karst  
94 systems and fault zones affected Cambrian dolomites. Exceptional outcrop conditions allowed  
95 to evidence a main mineralizing event during Late Permian syn-rift burial identified as a  
96 MVT ore deposit (Laurent, 2015; Laurent et al., 2017). In addition, polymetallic deposits are  
97 entrapped within meteoric karsts developed very close to the Middle Triassic post-rift  
98 unconformity of the basin and sealed by evaporitic marls (Lopez, 1992). The question here is  
99 whether the post-rift episode of barite and sulfide mineralization is related to a hydrothermal  
100 fluid circulation, as for the Late Permian metallogenesis, or a diagenetic remobilization of the  
101 previous ore deposits? We propose here a detailed study of the depositional environment and  
102 karst dynamics during the post-rift mineralizing event supplemented by a multi-scale analysis

103 of textures, mineralogy, fluid inclusions and radiogenic/stable isotopes (sulfur and strontium)  
104 on mineralized markers. The objectives of this study will be to (i) constrain the link between  
105 the sedimentary infill of meteoric karsts and ore trapping (ii) define the diagenetic  
106 transformations, the different fluid events and associated stages of mineralization that follow  
107 the post-rift exhumation of the basin, and (iii) understand the origin of metals as well as the  
108 sulfur cycling in the system and its role in the timing and location of polymetallic deposits. *In*  
109 *fine*, this multidisciplinary approach allows us to propose an integrated model of economic  
110 metals trapping few meters below the SWI and to discuss the interconnection between karst  
111 dynamics, playa lake environment and hydrocarbon dysmigration.

112

113

## 114 **2. Geological settings**

### 115 **2.1 Geodynamic evolution of the Lodève Basin**

116 The Lodève Basin, located 50km northwestern of Montpellier in the south of the  
117 French Massif Central, is a 180 km<sup>2</sup> cuvette-shaped half graben (Fig.1A). The half-graben  
118 geometry of the basin is linked to a gravitational collapse along the Hercynian mountain chain  
119 from Late Carboniferous to Late Permian (Echtler and Malavieille, 1990). The series shows  
120 an overall 15-20° southward dipping continental infilling bounded in the south by a north  
121 dipping listric normal fault related to an inversion of a main thrust during the Late Hercynian  
122 collapse (Lopez et al., 2008) (Fig.1B). During this phase, the progressive tilting of the basin  
123 was accommodated at the hinge of the roll-over anticline by the development of an E-W  
124 trending synthetic and antithetic fault corridor (Lopez, 1992; Wibberley et al., 2007; Laurent  
125 et al., 2017; Fig.1A and 1B). Middle Triassic terrestrial deposits unconformably seal an  
126 erosive surface truncating both the Late Carboniferous-Permian half graben and its basement

127 at the southern and northern basin margins (Fig. 1B). This post-rift unconformity marked the  
128 end of the Late Hercynian tectonics followed by a major regional erosion during which at  
129 least 1500m of Permian deposits were eroded, representing a gap of 15Myr (Lopez, 1992;  
130 Laurent, 2015). The Mesozoic period corresponds to a major change of the tectonic regime  
131 with the opening of the South-East basin, where the Lodève area corresponds to the western  
132 continental high margin controlled by NE-SW trending faults. The complete sealing of the  
133 residual Paleozoic reliefs is then linked to the overall extension of shallow marine carbonate  
134 deposits during Jurassic. Jurassic series are today preserved on the Causse du Larzac plateau,  
135 which was uplifted during the Cenozoic with the regressive entrenchment of the river  
136 networks.

137

## 138 **2.2 Stratigraphy of the Lodève Basin**

### 139 *The Hercynian basement*

140 In the northern margin of the basin, the Stephano-Permian series onlap unconformably  
141 the large wavelength folded and partly thrusted Cambrian basement at the hinge point of the  
142 roll-over anticline (Lopez, 1992). The major part of the Cambrian deposits corresponds to  
143 thick massive dolomite interbedded with thin calcschist layers. These carbonates are  
144 intensively fractured and suffered a severe karstification and canyon entrenchment during the  
145 Late Hercynian subaerial exposure.

146

### 147 *Syn-rift deposits (Stephano-Permian series)*

148 The Stephanian sedimentary deposits, which are only visible in the westernmost part  
149 of the basin (Graissessac sub-basin) and evidenced at depth by older exploration drillholes  
150 (Lod 2 projected drillhole in Fig.1B), are composed of thick coarse alluvial fan deposits at the

151 base, passing upward to coarse fluvial sandstones and muddy swamp to peat clay formations.  
152 Above Stephanian series, the Permian deposits have been divided into two large  
153 megasequences: the Autunian Group and the Saxonian Group (Gand et al., 1997). The  
154 Autunian Group is composed of a 700m-thick isopachous series of deltaic sandstones  
155 evolving upward into deep anoxic lacustrine black shales with high potential source rock for  
156 hydrocarbon (Laurent, 2015) and interlayered with laterally continuous volcanic ash layers  
157 (Odin, 1986). The Saxonian Group lies unconformably on the Autunian deposits and displays  
158 a clear divergent pattern that marks the main southward tilting of the Hercynian basement  
159 along the south bordering listric fault. The thickness of the Saxonian Group is estimated to  
160 3000m at present day but has certainly reached 5000m during the syn-rift subsidence of the  
161 basin (Laurent, 2015). It shows alluvial fan conglomerates passing rapidly to thick floodplain  
162 red pelites interbedded with thin blue-green playa lake mudstone deposits.

163

164 *Post-rift deposits (Middle Triassic series)*

165 The Middle Triassic deposits seal respectively the Permian in the southern and  
166 western part of the basin and the Cambrian and Precambrian basement in the northern part  
167 (Fig.2A and 2B). It consists of a 250m-thick pile composed of sandstone, mudstone and  
168 evaporite deposits, topped by mixed siliciclastic-carbonate facies at the transition with the  
169 Early Jurassic series. The series can be subdivided into four main formations according to  
170 their facies assemblage (Lopez and Mader, 1992; Fig.2C). The Lower Formation corresponds  
171 to the first 120m and shows typical Buntsandstein facies reported to the period from Anisian  
172 to Ladinian. It is mainly composed of fluvial sandstones passing to playa lake mudstone and  
173 evaporite deposits and vice-versa in a symmetrical megacycle. The Middle and Upper  
174 Formation (about 40m-thickness each one) show the same Keuper facies assemblage with a

175 basal 3-5 m-thick dolomite layer (key beds [a] and [b] in Fig.2C) capped by mudstones and  
176 gypsum/anhydrite/dolomite interbeddings developed in shallow littoral sabkhas. The Rhaetian  
177 Formation on top of the Triassic pile (Upper Norian) is characterized by mixed siliciclastic-  
178 carbonate facies (Lower Unit in Fig.2C) passing upward to pure ooidal and bioclastic  
179 grainstone-packstone deposits related to a shallow subtidal platform environment (Upper Unit  
180 in Fig.2C).

181

### 182 **2.3 Metallogenesis of the basin**

183         The Lodève basin was the site of two episodes of barite-sulfide ore deposition, the first  
184 during the Late Permian syn-rift structuring (Laurent et al., 2017) and the second following  
185 the post-rift exhumation during the Middle Triassic. During the syn-rift phase, the Lodève  
186 Permian basin experienced a long period of differential subsidence that led to a northward  
187 basinal fluids migration at the interface between Cambrian dolomites and the Lower Permian  
188 unconformity (Lopez, 1992; Laurent et al., 2017). Metal-rich dewatering fluids sourced in the  
189 Autunian blackshales and ash layers and moved under thermal and pressure gradient below  
190 the Early Permian seal to be accumulated at the hinge point of the roll-over anticline in the  
191 northern part of the basin (Lopez, 1992; Laurent, 2015; Laurent et al., 2017). Fluids were  
192 released and trapped along the active E-W compensation fault network, leading to  
193 polymetallic barite-sulfide (Pb, Cu, Zn) veins in fault zone and paleokarst cavities (Lopez,  
194 1992; Laurent et al., 2017). During Late Permian, the Autunian blackshales of the deepest part  
195 of the basin reached the oil window and led to hydrocarbon migration according to the same  
196 pathway and hydrodynamical conditions than prior metal-rich fluids (Laurent, 2015). Several  
197 oil seeps are still visible at the contact between the Early Permian series and the Cambrian

198 basement (Lopez and Petit, 2003). This fluid event was characterized as a typical MVT ore  
199 deposits linked to sediment dewatering during basin burial (Laurent et al., 2017).

200 Close to the post-rift unconformity marking the general exhumation of the entire basin,  
201 different barite-sulfide deposits were identified in the rejuvenated Cambrian paleoreliefs  
202 sealed by evaporitic marls in the northern part (Fig.2B and 2C; Lopez, 1992; Lopez, 1993).  
203 These ore deposits which may result from a distinct mineralizing episode than the syn-rift  
204 mineralizations are the focus of this paper.

205

206

### 207 **3. Materials and methods**

#### 208 **3.1 Geological mapping and field studies**

209 The main work was conducted in the hanging wall of the Olmet normal fault on the  
210 right bank of the Lergue River in the northern part of the basin where the lower formation of  
211 the Middle Triassic onlaps unconformably the Cambrian basement (Fig.1, 2A and 2B). A de-  
212 tailed geological map of the studied area was first carried out for the purpose of locating and  
213 clarifying the main ore deposits and facies distribution along the major post-rift unconformity  
214 (Fig.2A and 2B). Ten main ore deposits (identified by the name of the place and letter from a  
215 to j in Appendix A) have been recognized and studied in this area. All these sites were care-  
216 fully studied and sampled in order to characterize the lithology of the studied site, the sedi-  
217 mentological assemblage and the fabric of the mineralized deposits. 4 main outcrops are de-  
218 scribed in detail in this paper (in bold characters on Appendix A).

219 Complementarily, Triassic evaporitic gypsum and anhydrite were sampled at the near-  
220 est accessible sites where this formation is accessible at outcrop (see Fig.1A for the location  
221 of samples).

222

### 223 **3.2 Petrography**

224 Textures and mineralogy of ore deposits have been observed from polished thin sec-  
225 tions using a Zeiss Scopa A1 optical microscope in transmitted and reflected lights at the Uni-  
226 versity of Montpellier (France). These observations were supplemented by Scanning Electron  
227 Microscopy and Energy Dispersive X-ray Spectroscopy (SEM-EDS) with a FEI Quanta 200  
228 Field Emission Gun of Schottky type.

229

### 230 **3.3 Fluid inclusion microthermometry**

231 Fluid inclusion microthermometry was performed on 100 $\mu$ m-thick double polished  
232 section using Linkam heating/freezing stage, mounted on a Leica microscope. The stage was  
233 calibrated according to synthetic fluid inclusions (Sterner and Bodnar, 1984) at temperatures  
234 of -56.6°C, 0.0°C and 374.1°C. The primary, pseudo-secondary and secondary nature of fluid  
235 inclusions assemblages were identified according to the criterion defined by Roedder (1984)  
236 and Bodnar (1985). In our study, only primary fluid inclusions were analysed reflecting the  
237 P/T/ $\chi$  properties of the mineralizing fluids such as (i) the homogenization temperature ( $T_h$ ), (ii)  
238 the first apparent melting temperature at which liquids first co-exist with solids related to  
239 eutectic temperature ( $T_e$ ) and (iii) the final ice-melting temperature ( $T_{mIce}$ ), when solids  
240 completely disappeared. The McFlinco program (Brown, 1989) was used to calculate the salt  
241 composition, the salinity and the density of the initial fluids (Bodnar, 1993; Duan et al., 1992).  
242 Finally, fluorescence X and Raman spectroscopy were used to identify potential hydrocarbon-  
243 rich fluid inclusions.

244

### 245 **3.4 Strontium concentration and isotopic composition**

246 Strontium isotopic composition of barites has been measured at Isotope Laboratory of  
247 BRGM (Orléans, France). Around 30-50mg of barite powder was partly dissolved in beaker  
248 with a solution of 10ml of 8N HCl which was heated at 100°C during 12 days. After  
249 centrifugation, the liquid is separated from the solid residue and the latter is dried and  
250 weighted. 5 to 15% of barite was dissolved. The liquid is then evaporated to recover the dry  
251 residue then mixed up with 0.3ml of 41N HNO<sub>3</sub> and diluted with ultrapure water. Normalized  
252 on the Sr content in samples, 2µg of Sr was dried and submitted to the purification chain. A  
253 chemical separation is then performed with the purification of the Sr using an ion-exchange  
254 resin (Sr-Spec) before mass analysis according to a method adapted from Pin and Bassin  
255 (1992) (total blank <1ng). For the analysis of <sup>87</sup>Sr/<sup>86</sup>Sr ratios, 150ng of Sr was loaded onto a  
256 tungsten filament with tantalum activator and analysed with a Finnigan MAT262 multi-  
257 collector solid source mass spectrometer. The internal precision obtained during the analyses  
258 is around ±10ppm (2σ<sub>m</sub>) according to repeated analyses of the NBS987 standard to test the  
259 reproducibility, with a mean value of <sup>87</sup>Sr/<sup>86</sup>Sr of 0.710246 ± 0.000010 (2σ, n = 18). Sample  
260 ratios are normalized to the certified value of the NBS987 (<sup>87</sup>Sr/<sup>86</sup>Sr= 0.710240).

261 The strontium concentration have been measured using the in situ laser ablation  
262 method LA-ICPMS (Laser ablation – Inductively Coupled Plasma Mass Spectrometry) on  
263 100µm-thick double polished sections, at Geosciences Montpellier (France). We used a  
264 Compex 102 excimer laser (LambdaPhysik) operating in the deep-UV, which is periodically  
265 infilling by an ultrapure ArF gas excited by 28 kV electric shock in order to associate the fluor  
266 with argon to form the ephemerial molecule ArF. As this molecule is unstable, the liberation  
267 of fluor atom induced a photonic ray with a wavelength of 193nm. The particles issued from  
268 the interaction between the laser and the samples are directed to the ICP-MS torch by a He



269 flux and then mix to argon. The ablation by He enhanced the sensibility of the mass  
270 spectrometer and reduced the interelementary variations (Günther and Heinrich, 1999). The  
271 quantification of elementary concentration of samples was realized through the repeated  
272 measurements on a silicate glass (NIST 612) containing around 40ppm of most trace elements.  
273 The control of the accuracy and precision of the analyses was based on natural reference  
274 materials of BIR (basaltic glass) and artificial type of MACS3 (carbonate pellet). Signals are  
275 analysed by a magnetic sector mass spectrometer Element XR (ThermoFinnigan). Finally,  
276 signal processing and concentration calculations were performed using GLITTER software  
277 (GEMOC – Van Aelterbergh et al., 2001).

278

### 279 **3.5 Sulfur isotopes**

280 Sulfur isotopes analyses of barites, gypsum and anhydrite were performed at the  
281 Institute of Earth Surface Dynamics of the University of Lausanne (Switzerland) using a  
282 Carlo Erba 1108 elemental analyser (EA, Fisons Instruments, Milan, Italy) connected to a  
283 Thermo Fisher (Bremen, Germany) Delta V isotope ratio mass spectrometer (IRMS) that was  
284 operated in the continuous helium flow mode via a Conflo III split interface (EA-IRMS). The  
285 stable isotope composition of sulfur is reported in the delta ( $\delta$ ) notation as the per mil (‰)  
286 deviation of the isotope ratio relative to known standards:  $\delta = [(R_{\text{sample}} - R_{\text{standard}})/R_{\text{standard}}] \times 1000$ , where R is the ratio of the major heavy to light sulfur isotopes  
287 ( $^{34}\text{S}/^{32}\text{S}$ ). The sulfur standard is the Vienna Cañon Diablo Troilite (V-CDT). Preparation of  
288 samples have been made according to the method presented in Spangenberg et al. (2010). The  
289 reference  $\text{SO}_2$  gas was calibrated against the IAEA-S-1 sulfur isotope reference standard  
290 ( $\text{Ag}_2\text{S}$ ) with  $\delta^{34}\text{S}$  value of -0.3‰. The overall analytical reproducibility of the EA-IRMS  
291 analyses, assessed by replicate analyses of three laboratory standards (synthetic cinnabar, with  
292

293 a working  $\delta^{34}\text{S}$  value of +15.5‰; barium sulfate, +12.5‰; pyrite Ch, +6.1‰; pyrite E, -7.0‰)  
294 is around  $\pm 0.2\text{‰}$  (1 SD). The accuracy of the  $^{34}\text{S}$  analyses was checked periodically by  
295 analyses of the international reference materials IAEA-S-1 and IAEA-S-2 silver sulfides (0.3‰  
296 and +22.7  $\pm 0.2\text{‰}$ , respectively, values from IAEA-Catalogue and Documents) and NBS-123  
297 sphalerite (+17.09  $\pm 0.31\text{‰}$ , value from NIST-Catalogue and Documents).

298 In addition, in situ sulfur isotope measurements on 23 chalcopyrites were made by  
299 Secondary Ion Mass Spectrometry (SIMS) equipped with a cesium source on CAMECA  
300 IMS5F at the University of Montpellier (France). The internal precision as well as the  
301 reproducibility of results was checked on laboratory standards of three chalcopyrites whose  
302  $\delta^{34}\text{S}$  signatures are respectively 4.4  $\pm 1.6\text{‰}$ , 3.47  $\pm 0.42\text{‰}$  and 2.29  $\pm 0.2\text{‰}$ , giving an  
303 analytical error inferior to  $\pm 1\text{‰}$ .

304

305

## 306 **4. Results**

### 307 **4.1 Architecture, mineralogy and texture of Middle Triassic ore deposits**

#### 308 **4.1.1 The Roche Percée paleo-pothole**

309 The site of Roche Percée is located close to the right bank of the Soulandres River in  
310 the western suburb of Lodève city (b in Fig.2A and Appendix A). The outcrop consists of an  
311 isolated dyke of mineralized and silicified breccias, largely exhumed from the surrounding  
312 rocks, and rooted into the Cambrian basement. Here the Triassic cover has been totally erod-  
313 ed.

314 The mineralized dyke displays a subvertical east-west trending wall of 40 m-long, 4m-  
315 wide and 8 to 12m-high entrenched parallel to the stratigraphic contact between beige massive  
316 dolosparite in the southern border and blue-grey calcschists in the northern side (Fig. 3A).

317 The dyke infill is bounded by a silicified wall penetrating both the Cambrian dolomites and  
318 the calcschists on a thickness of about 10 to 20cm and even reaching 4m in the northwestern  
319 slab (Fig. 3B and 3C). Moreover, angular centimetre to pluri-decimetre-size blocks of silici-  
320 fied wall are visible in the dyke infill, indicating that the major stage of silicification preceded  
321 the mineralization. Three main facies, called respectively RP1, RP2 and RP3, have been ob-  
322 served in the dyke infill:

323       **- RP1 Facies:** this facies consists of a black organic matter- and silica-rich pyrite bear-  
324 ing mudstone forming the northward inclined slab in the northwestern part of the outcrop  
325 (Fig. 3A and 3B). This facies is thinly laminated with lighter fine siltstone laminae alternating  
326 with dark organic-rich and highly silicified mudstone laminae;

327       **- RP2 Facies:** composing the main dyke infill, the RP2 Facies is a well stratified pluri-  
328 centimetre- to decimetre-thick barite-rich beige siltstone forming undulated bedsets with mul-  
329 tiple low-angle truncations (Fig.3B, 3C, 4A and 4B). Perpendicular sections of the dyke show  
330 a clear concave shape pattern of the bedsets attesting to a collapse during the phase of infil-  
331 ling. In thin section, the RP2 Facies shows a particularly remarkable stacking of millimetre- to  
332 centimetre-thick graded couplets including a silt and sand-size grains with discrete barite  
333 crystals plates, passing upward to brown dolomitic siltstone (Fig.4C). Barite plates are often  
334 broken and corroded (Fig.4D). Plates are progressively more abundant to the top forming  
335 massive barite laminae of millimetre- to centimetre-size fibro-radiated spherules. Locally,  
336 speckles and blebs of galena, chalcopyrite and gray copper are dispersed in barite (Fig.4E).

337       **- RP3 Facies:** the RP2 Facies is overlaid or passes laterally to massive mud-supported  
338 breccia, composing the RP3 Facies (Fig.3B and 3C). The breccia consists in centimetre- to  
339 pluri-decimetre size angular clasts of calcschists, dolomites and silicified surrounding rocks  
340 floating into barite-rich siltstone to fine sandstone (upper part of Fig.4A). In some places, both

341 the RP2 and RP3 Facies display centimetre-size craters linked to gypsum-anhydrite dissolu-  
342 tion (Fig.4A).

343

#### 344 **4.1.2 The Olmet Road paleo-lapiaz network**

345 Along the Olmet Road (f in Fig.2A and Appendix A), an outcrop consists in a fault-  
346 controlled Cambrian paleorelief partly onlapped by sandstones and marls belonging to the  
347 Lower Formation of the Middle Triassic (Fig.2C and 5A). The main outcrop forms an  
348 irregular 2.5 to 6m-high and 45m-long ENE-WSW trending escarpment. The vertical  
349 succession shows in the upper part of the outcrop massive to roughly bedded Cambrian  
350 dolomites with a general dip of about 80° to the south, unconformably onlapped by bluish  
351 evaporitic marls and fine to very fine yellowish sandstones moulding the karstified paleorelief  
352 (Fig. 5A). The intermediate part of the outcrop is characterized by a blurred and very irregular  
353 orange to dark brown colored interval partly masking the surface of unconformity because of  
354 the intense impregnation by limonites, goethite and hematite. This oxidized front has a  
355 thickness ranging from about 1 to 4m according to the depth of karstification. Careful  
356 observation of this interval shows that the beige-colored Cambrian dolosparites progressively  
357 assumes upward a brown color with an increase in iron carbonate and silica content. In  
358 parallel to paleo-lapiaz infill, silicified sulfide-impregnated subvertical bed-controlled bands  
359 develop locally several meters below the paleosurface. The western part of the outcrop is  
360 crossed by a NW-SE trending normal fault showing a throw of about 4m toward the North-  
361 East.

362 Barite-sulfides mineralizations are covered by alternations of bluish gypsum-rich  
363 marls and fine partly silicified sandstones (Fig.5A and 5B). Three types of mineralizations  
364 have been observed below the unconformity surface, from the base of the outcrop to the

365 paleosurface: (i) pluri-centimetre-thick massive barite veins, without sulfides, dispersed in the  
366 Cambrian dolomites with a random distribution; (ii) connected to the paleosurface, subvertical  
367 pluri-decimetre-thick partly oxidized bed-parallel pyrite veins and sulfide-rich impregnations  
368 of the Cambrian dolomites (Fig.5B); and (iii) the main ore facies consists in a complete  
369 mineralized sedimentary infill all along the irregular karstic paleosurface affected by paleo-  
370 lapiaz. In the central part of the outcrop, this main ore facies forms a laminated sulfide-rich  
371 bluish vadose silty claystone including brown patches of iron oxides associated with barite  
372 pockets (Fig.5A and 5C). This mineralized interval is capped by a 1m-thick brown sulfide-  
373 rich siltstone to very fine sandstone, partly silicified sealing the karstic Triassic unconformity.  
374 This facies is several meters-thick and fills completely the karstic cavities in the eastern and  
375 western part of the outcrop. The mineralized suite include dispersed blebs and speckles of  
376 galena, sphalerite and grey copper filling the intergranular porosity and forming thin veins or  
377 platings associated to secondary copper and lead carbonates, barite and bitumen blebs. As this  
378 facies is really representative to the Middle Triassic mineralizing event, we name this deposit  
379 OR Facies in the following.

380

#### 381 **4.1.3 The Montifort Road planar cavities string**

382 This ore deposit is located along the Montifort road to Olmet village in the south sub-  
383 urb of Lodève city (a in Fig.2A and Appendix A). Here the Cambrian blue-grey calcschists  
384 dip 75° to the south and are unconformably covered by the Middle Triassic deposits (Fig.6A).  
385 The Triassic unconformity is clearly irregular with decimetre-large potholes sealed in onlap  
386 by very fine brown sandstones and evaporitic marls interbeddings. About 1 to 1.5m below the  
387 unconformity, the calcschists are intersected by superposed strings of interconnected planar  
388 cavities parallel to the unconformity surface and partly filled with barite and brown fine

389 grained silts (Fig.6A and 6B). The size of the planar cavities is comprised between a few cen-  
390 timetre to a few decimetre. They are surrounded by a sub-vertical fracture network developed  
391 in bedding planes, enlarged by karstification process and sometimes infilling by vadose sedi-  
392 ments. As observed in the Roche Percée paleo-pothole, the planar cavities string and associat-  
393 ed veins are accompanied by an intense silicification of the surrounding calcschists penetrat-  
394 ing the walls from about 10 to 20cm with red-coloured chalcedony development (4 in Fig.  
395 6B). The planar cavities display a geopetal fabric with carbonate granules and siltstone sealed  
396 locally by barite blocky cement (Fig. 6C and 7AD). The granules infilling the cavities show a  
397 particularly relevant reverse grading with a size ranging from 100 $\mu$ m at the base to a few mil-  
398 limetre at the top (Fig. 6B and 6C). Granules are rounded and composed of dolomudstone-  
399 supported silts (Fig.7A). Laterally within the infilling, granules pass to more homogeneous  
400 sediments constituting mud with curved cracks. In thin section, the fine-grained sediment and  
401 associated granules are mainly composed of dolomudstone-supported silt including quartz and  
402 iron oxides. Very fine-grained silt (20 to 100 $\mu$ m) partly fills the intergranular space with a  
403 geopetal pattern. On cross polarized light microscopy, the granules show a partial penetrative  
404 silicification with the development of quartzine spherulites tending to evolve into microquartz  
405 (Fig.7A). The residual intergranular voids are upholstered with drusy megaquartz that can  
406 close completely the remaining space (Fig.7B).

407         The barite and accessory sulfide cement developed discontinuously above the granule-  
408 siltstone infill. The contact is erosional with a very irregular sharp and underlined by pluri-  
409 millimetre-thick brown ankerite (Fig.6C, 7B, 7C). This mineralized facies is mentioned as  
410 MR1 Facies in the following. Fluorescence X observations reveal a high content of organic  
411 matter-rich patches within and along crystal faces of ankerite at the contact with barite crys-  
412 tals (Fig.7D). Locally, the intrakarstic sedimentary infill is brecciated and incorporated as re-

413 sidual clasts or blocks in the barite cement. The barite develops as fan shaped cockade clus-  
414 ters corresponding to the growing of large slats in an open space (Fig.6C and 7C). Close to the  
415 contact with barites, pyrites, galena and sphalerite patches are present, always cemented by a  
416 late sparitic calcite (Fig.9E) and often associated with bitumen bubbles and blebs trapped in  
417 residual voids.

418 Two hundred meters north-eastward along the main road, the Cambrian dolomites are  
419 unconformably overlapped by the basal conglomerate of the Early Permian dipping 25° to the  
420 North (outcrop j on Fig.2A and Appendix A). The conglomerates are themselves capped hori-  
421 zontally by the Middle Triassic sandstone and marl alternations. Here the Cambrian dolomites  
422 and basal conglomerates are crossed by multiple barite and grey copper/chalcopyrite veins  
423 and hydraulic breccia without any link with the overlying Triassic unconformity. This miner-  
424 alized fabric, called here as MR2 Facies, is similar to the Late Permian MVT ore deposits de-  
425 scribed by Laurent et al. (2017).

426

#### 427 **4.1.4 The Belbezet karstic mine**

428 This site corresponds to an old mining work exploited during the roman period for  
429 copper and silver. The main mining gallery is carved in the mineralized interval along the  
430 basal unconformity on the flank of a paleorelief between the Cambrian dolomites at the  
431 footwall and a debris-flow conglomerate at the hanging wall (e in Fig.2A, Fig.8A and 8B).  
432 The stratigraphical contact shows a general dip of about 35° to the South-West. The debris-  
433 flow conglomerate is about 2m-thick and includes numerous pebble-sized dolomite blocks  
434 floating into a sandy matrix. It is capped by blue-green marls alternating with thin very fine  
435 sandstone layers including pseudomorphs after anhydrite. The paleosurface includes metric  
436 paleo-potholes associated with an open-fracture network descending several decimetres to

437 several meters below the unconformity and including pluri-decimetres blocks brecciated in  
438 situ and intrakarstic infill.

439 The mineralized interval (BM Facies) fills the cavities network with a very variable  
440 thickness. It is composed of sulfide-barite-rich silty-clayey matrix packing within  
441 heterometric Cambrian blocks (Fig.8B and 8C) and passing upward to massive white barite  
442 (Fig.8A and 8B). Barites are locally highly sheared and also injected by grey copper sulfides,  
443 chalcopyrites and abundant bitumen droplets and heavy oil that totally stain the barite in grey  
444 (Fig.8D).

445

## 446 4.2 Fluid inclusion petrography and microthermometry in barites

### 447 4.2.1 Petrography of fluid inclusions

448 The fabric of primary fluid inclusions in barite within the MR2 Facies, from the  
449 northern part of the Montifort Road outcrop, displays a two-phase assemblage with an oblong  
450 geometry positioned along growth zones and a size between 10 and 40 $\mu$ m. We have  
451 intentionally excluded fluid inclusions close to the cleavage planes as barite is very sensitive  
452 to post-crystallization deformation (Ulrich and Bodnar, 1988). The R<sub>v</sub> (ratio between vapor  
453 and vapor+liquid) is ranging between 10 and 20%.

454 Entrapped within blocky barites of the MR1 Facies from the Montifort Road planar  
455 cavities string, we observed two generations of primary fluids inclusions: two-phase  
456 inclusions with R<sub>v</sub> of 20 to 30% close to the centre of the crystal and stable single-phase  
457 liquid inclusion along the external face (Fig.9A). Secondary inclusions are also identified with  
458 a higher R<sub>v</sub>, between 50 and 60%, a larger size, and evidences of post-trapping deformation  
459 such as necking-down. Very few and small hydrocarbon-rich fluid inclusions were identified  
460 by fluorescence X despite the fact that oil and bitumen is clearly visible in the mineralized



461 facies. Raman analyses were not discriminating, because of the high fluorescence of the  
462 samples linked to the important content of oil impregnations in barites.

463 Fluid inclusions entrapped within the rhythmic infilling of the Roche Percée paleo-  
464 pothole (RP2 Facies) and the barite from the Olmet Road paleo-lapiaz (OR Facies) are  
465 essentially stable single-phase liquid inclusions and very small in size considering the fine  
466 barite crystallites (Fig.9B). Even during cooling of samples, no gas bubbles have nucleated in  
467 these inclusions. Consequently, no microthermometry have been performed on these  
468 mineralized facies.

469

#### 470 **4.2.2 Microthermometry**

471 The results of microthermometry ( $T_e$ ,  $T_{mIce}$  and  $T_h$ ) for all selected ore facies are  
472 presented on Table 1 and Figure 10.

473 The primary fluid inclusions in the MR2 Facies of Montifort Road show a majority of  
474 homogenization temperatures in the range of 180-200°C. The  $T_e$  are between -30 and -20°C,  
475 for an average of -24°C, indicating that the mineralizing fluid is an H<sub>2</sub>O-NaCl brine with a  
476 low proportion of Ca<sup>2+</sup> (from -22.9°C: Crawford, 1981; from -21.2°C: Borisenko, 1977). The  
477  $T_{mIce}$  are characterized by a wide distribution of values for an average of -8.77°C,  
478 corresponding to a salinity of 12.6 wt%eq.NaCl (Brown and Lamb, 1989) and a density of  
479 0.987 (Bodnar, 1994).

480 For the MR1 Facies within the Montifort Road planar cavities string, primary two-  
481 phase inclusions have lower homogenization temperatures, mostly in the range of 60 to 80°C  
482 for a mean value of 77°C. The modal values of  $T_e$  and  $T_{mIce}$  are between -25/-20 °C and -  
483 12/-10°C respectively, corresponding to an average salinity of 13.56 wt% eq.NaCl and a  
484 density of 1.069.

485

### 486 **4.3 Sulfur and strontium geochemistry**

487 Strontium concentration and strontium isotopes ( $^{87}\text{Sr}/^{86}\text{Sr}$ ) analyses on barite of the  
488 three main textural facies (RP2, MR1 and BM) were performed associated to sulfur isotopes  
489 ( $^{34}\text{S}/^{32}\text{S}$ ) measurements on both barites and chalcopyrites evidenced within a same facies.  
490 Similar sulfur isotopes analyses have been made on chalcopyrites in a fourth sample of  
491 mineralization from the Olmet Road (OR Facies) and also in evaporites belonging to the  
492 Middle to Upper Triassic formations (EV1 and EV2 Facies). A comparison with the isotopic  
493 signatures of Late Permian barites and sulfides presented in Laurent et al. (2017) was also  
494 carried out in order to determine a potential geochemical inheritance (Table 2).

495

#### 496 **4.3.1 Ba-Sr concentration and strontium isotopes in barites**

497 The Sr concentration in barites close to the Triassic post-rift unconformity ranges from  
498 4400 and 11800ppm, far away from the barites attributed to the Late Permian in Laurent et al.  
499 (2017) that ranges from 19500 to 43803ppm (Table 2).

500 Figure 11 shows the  $^{87}\text{Sr}/^{86}\text{Sr}$  values as a function of strontium concentration for  
501 Middle Triassic barites compared to the signature of the three ore generation of Late Permian  
502 barites identified in Laurent et al. (2017). The strontium isotopic signature of the barites  
503 composing the RP2 Facies is significantly lower than all other barites with a value of 0.70888,  
504 but very close to the general value of Triassic evaporites which ranges between 0.70745 and  
505 0.70795 after Koepnick et al. (1990) and up to 0.7086 after Song et al. (2015). The  $^{87}\text{Sr}/^{86}\text{Sr}$   
506 values between 0.71139 and 0.71142 for BM and MR1 Facies respectively are close to the  
507 signatures of the first and second generations of Late Permian barites.

508

### 509 4.3.2 Sulfur isotopes of barites, chalcopyrites, evaporitic gypsum and anhydrite

510 As chalcopyrites are often associated with barites in all ore facies studied in this paper,  
511 we use the difference of  $\delta^{34}\text{S}$  between barite and associated chalcopyrites in a same facies  
512  $\delta^{34}\text{S}_{\text{barite}} - \delta^{34}\text{S}_{\text{chalcopyrite}}$ , annotated  $\varepsilon^{34}\text{S}$ , which may be representative of the fractionation of  
513 sulfur isotopes during the precipitation of the barite-sulfide front. All results of sulfur isotopic  
514 composition are synthetized in Table 2.

515 We obtained values of  $\delta^{34}\text{S}$  of +13.7 and +14.79‰ V-CDT for the Triassic evaporitic  
516 gypsum (EV1 Facies) and of +14.6 and +14.9‰ V-CDT for the Triassic evaporitic anhydrite  
517 (EV2 Facies).

518 For the Middle Triassic barites, the  $\delta^{34}\text{S}$  of OR and RP2 Facies ranges between +15.7  
519 and +16.2‰ V-CDT and are slightly superior for the mineralizations corresponding to the  
520 MR1 and BM Facies with  $\delta^{34}\text{S}$  values between +16.2 and +18.5‰ V-CDT. For all Middle  
521 Triassic barites,  $\delta^{34}\text{S}$  values are higher than the Triassic evaporites but mostly similar to the  
522 Late Permian barites which signatures range between +15.6 and +18.4‰ V-CDT (Laurent et  
523 al., 2017).

524 The  $\delta^{34}\text{S}$  for Middle Triassic chalcopyrites is different from Late Permian sulfide de-  
525 posits ( $\delta^{34}\text{S}$  between -15 and -5‰ V-CDT; Laurent et al., 2017) with two distinctive domains:

526 (i) negative  $\delta^{34}\text{S}$  values for RP2 and OR Facies, ranging respectively from -2.1 to -  
527 1.4‰ V-CDT and from -7.2 to -1.7‰ V-CDT. For these facies, the difference of  $\delta^{34}\text{S}$  be-  
528 tween barite and chalcopyrites  $\varepsilon^{34}\text{S}$  ranges between +17.1 and +23.4‰ V-CDT, representing  
529 an important fractionation of sulfur isotopes during the precipitation.

530 (ii) positive  $\delta^{34}\text{S}$  values in BM and MR1 Facies. The BM Facies shows  $\delta^{34}\text{S}$  varying  
531 between +11.9 and +17.1‰ V-CDT, close to the Triassic evaporites signatures, and are char-  
532 acterized by a very week  $\varepsilon^{34}\text{S}$  ranging from +4.8 to -0.9‰ V-CDT. The MR1 Facies has a

533  $\delta^{34}\text{S}$  of +18.9‰ V-CDT, for a  $\epsilon^{34}\text{S}$  of -0.4 and -2‰, thus close to 0‰ if we consider the ana-  
534 lytical error of around 1‰ for SIMS measurements.

535 Even though some chalcopyrites are considered to be synchronous with barites accord-  
536 ing to the petrographic study, we did not consider an isotopic equilibrium between these two  
537 phases. Indeed, the temperatures calculated according to the Rye and Ohmoto (1974) and  
538 Ohmoto and Lasaga (1982) equations give aberrant precipitation temperature values (superior  
539 to 250°C) in comparison with those obtained by microthermometry.

540

541

## 542 **5. Discussion**

### 543 **5.1 Timing and origin of mineralizing fluids**

544 Field observations supported by fluid inclusions microthermometry and  
545 sulfur/strontium isotopes analyses clearly indicate two main types of mineralization trapped in  
546 the Cambrian paleokarst just below the Middle Triassic unconformity (Fig.11).

547 The early mineralization includes anhedral sulfides (pyrite, chalcopyrite, galena and in  
548 less proportion sphalerite and tetrahedrite) that precipitated into void spaces of sheaf-like and  
549 massive barite composing the intrakarstic sediments of the Roche Percée paleo-pothole (RP2  
550 and RP3 Facies) and of the exokarst observed in the Olmet Road outcrop (OR Facies). The  
551 alternation of barite and intrakarstic sediments in karstic cavities and the presence of  
552 allochthonous corroded and broken barite crystals in the RP2 Facies indicates their  
553 synsedimentary precipitation origin and hydrodynamic transportation during water table  
554 fluctuation in the karst. For convenience, we named this event Type I mineralization.

555 A second type of barite-sulfides deposits has been observed associated with  
556 hydrocarbon and mineralized few meters below the water table in endokarst network. They

557 were particularly observed at the Montifort Road outcrop and Belbezet Mine and include  
558 euhedral sulfides (pyrite, chalcopyrite and galena) trapped into cockade-shaped barite for the  
559 first area (MR1 Facies) and disseminated into a silty clayey matrix from the second zone (BM  
560 Facies). The ore deposits related to this event is called Type II mineralization.

561           Complementarily, the barite of the MR2 Facies, sampled in a sub-vertical vein distant  
562 from the post-rift unconformity, are characterized by higher homogenization temperature  
563 (between 139 and 195°C) of primary fluid inclusions than for the Type I and Type II  
564 mineralizations (between 49 and 102°C) (Fig.10 and Table 1). Such fluid characteristics are  
565 very similar to the ore facies described for the Late Permian MVT episodes by Laurent et al.  
566 (2017). Consequently, we attributed these veins as a prior mineralizing event regarding the  
567 Middle Triassic mineralizing episodes.

568           Knowing that strontium isotopes do not fractionate below 400°C (Matter et al., 1987),  
569 the  $^{87}\text{Sr}/^{86}\text{Sr}$  of barites reflects the strontium isotopic composition of the source. In our case,  
570 strontium isotopic signatures suggest two different sources of metals for Type I and Type II  
571 mineralizations (Table 2 and Fig.12). The  $^{87}\text{Sr}/^{86}\text{Sr}$  value of 0.70888 of barites of the Type I in  
572 the Roche Percée paleo-pothole (RP2 Facies) is compatible with the direct participation of Sr  
573 and associated Ba derived from the underlying Middle Triassic playa lake aquifer as the  
574 signature is very similar to Triassic evaporites ( $^{87}\text{Sr}/^{86}\text{Sr}$  between 0.70745 and 0.70795 after  
575 Koepnick et al. (1990) and up to 0.7086 after Song et al. (2015)). This direct connection  
576 between the karst and the overlying depositional environment is also supported by the  
577 synsedimentary features of mineralizations. On the contrary, the strontium isotopic signatures  
578 of barites at the Belbezet Mine and Montifort Road outcrops (BM:  $^{87}\text{Sr}/^{86}\text{Sr}$  of 0.71139; MR1:  
579  $^{87}\text{Sr}/^{86}\text{Sr}$  of 0.71142), constituting the Type II mineralizations, are much more radiogenic than

580 Triassic evaporites (Fig.12) which preclude a direct link with the sulfate-rich lake waters and  
581 rather suggest an external source of metals.

582 In the MR1 Facies, the high Th of fluid inclusions in barites, between 42 and 102°C,  
583 and an elevated salinity (Fig.10), do not correspond to an early diagenetic stage close to the  
584 SWI and necessarily involved the migration of deep basinal brines. The involvement of  
585 basinal brines is supported by the systematical association of barites of the Type II and  
586 hydrocarbon markers indicating that the petroleum system was still active during the Middle  
587 Triassic. However, if the barite crystal initiated during deep basinal fluid migration, the  
588 presence of single-phase liquid inclusion in the late stage of barite growing suggests that the  
589 crystal development finalized within a low-temperature water (Goldstein and Reynolds, 1994).  
590 Even if, the presence of oil in the Type II mineralization could indicate that the Middle  
591 Triassic metallogenesis may be a simple continuation of the previous Late Permian fluid  
592 migration (Laurent et al., 2017), we suggest that both episodes are decoupled. The cessation  
593 of fluid migration linked to the 1500m post-rift exhumation of the basin margin during the  
594 Middle Triassic (Lopez, 1992; Lopez et al., 1998; Laurent, 2015) is supported by the different  
595 strontium isotopic signature between Middle Triassic barites and the latest generation of the  
596 Late Permian Barites (Fig.12) (Laurent et al., 2017). The  $^{87}\text{Sr}/^{86}\text{Sr}$  of the Type II barites are  
597 very close to the barites associated with the first and second Late Permian fluid events  
598 occurring in the Lodève Basin (Laurent et al., 2017) suggesting that metals for Type II  
599 mineralizations were derived from the remobilization of previous barite-sulfide mineralization.  
600 In addition the drastic decrease in the Sr concentration in the Middle Triassic barite (Fig.12) is  
601 typical of the leaching of anterior barites by undersaturated water (Gordon et al., 1954; Cohen  
602 and Gordon, 1961; Renault and Brower, 1971).

603

## 604 5.2 Ore trapping redox conditions

605 As demonstrated previously, strontium isotopic signatures of Type I barites confirm  
606 that the most valuable source of sulfur is the playa lake environment linked to semi-arid  
607 climate conditions. The high sulfur isotopes fractionation between Type I barite-sulfide  
608 deposits and the Triassic evaporites may indicate a process of BSR (Machel et al., 1995). In  
609 this case, we assumed that dark organic-rich facies infilling karstic cavities at the Roche  
610 Percée paleo-pothole (RP1 Facies) and local abundance of plants and wood debris in the basal  
611 debris-flow deposits at the Belbezet Mine could represent the source methane, necessary to  
612 bacteria metabolism. The presence of only primary single-phase liquid fluid inclusions  
613 indicates low-temperature precipitation, below 50°C (Goldstein and Reynolds, 1994) (Table  
614 2), compatible with the BSR reaction which is stopped around 80°C (Postgate and Schwartz,  
615 1985). The high values of the  $\epsilon^{34}\text{S}$ , between 17.1 and 23.4‰ V-CDT (Fig.13 and 14), is  
616 consistent with the process of BSR development in a closed-system for sulfate supply  
617 (Harrison and Thode, 1958; Ohmoto, 1990; Canfield, 2001; Wortmann et al., 2001; Lerouge  
618 et al., 2011).

619 In the case of the Type II mineralization (MR1 and BM Facies), the  $\delta^{34}\text{S}$  of sulfides  
620 show an important  $^{34}\text{S}$  enrichment with  $\delta^{34}\text{S}$  reaching the value of Triassic evaporites and  
621 synchronous barites (Fig.13 and 14). High values of  $\delta^{34}\text{S}$  in sulfides in a low temperature sul-  
622 fate-rich environment are generally attributed to the development of a SMTZ associated with  
623 a process of anaerobic oxidation of methane coupled with bacterial mediated sulfate reduction  
624 (AOM-SR). As explained in the introduction, the SMTZ is a redox boundary resulting from  
625 the coeval activities of sulfate-reducing bacteria and anaerobic methanotropic Archaea (Ree-  
626 burgh, 1976; Alperin et al., 1988; Hoehler et al., 1994; Borowski et al., 1997; Borowski et al.,  
627 1999; Aloisi et al., 2000; Dickens, 2001; Niemann et al., 2006; Knittel and Boetius, 2009). At

628 the depth of SMTZ, AOM is responsible for the production of a significant amount of dis-  
629 solved  $\text{HS}^-$  and because the interstitial sulfate is really enriched in  $^{34}\text{S}$  at this depth, the reac-  
630 tion between dissolved sulfur and metals results in the precipitation of  $^{34}\text{S}$ -rich sulfides com-  
631 pared to sulfides in the overlying sulfate reduction zone which is submitted to BSR, as it is the  
632 case for the Type I mineralization. A crucial element in our study area is the migration of hy-  
633 drocarbon contemporaneous to the Type II mineralizations. Consequently, we assume that, at  
634 the time of a permanent shallow lake environment, a downward diffusion of sulfates toward  
635 the karst network and the rise of deep hydrocarbons in the Cambrian basement were condu-  
636 cive to the formation of a SMTZ (Fig.14). The undersaturation in  $\text{SO}_4^{2-}$  below the SMTZ  
637 caused the dissolution the Late Permian barite-sulfide deposits thus constituting the main  
638 source of sulfate and barium for the Type II mineralizations, as also demonstrated by the simi-  
639 lar strontium isotopic signature between Type II and Late Permian barites. When hydrocar-  
640 bons reached the SMTZ, the increase of alkalinity in the solution caused the formation of au-  
641 thigenic carbonates (Moore et al., 2004; Raiswell and Fisher, 2004; Meister et al., 2007) as  
642 evidenced by the hydrocarbon-rich ankerite minerals systematically surrounding the minerali-  
643 zations in the endokartic cavities. Neo-formed barite forming at SMTZ is not so  $^{34}\text{S}$ -enriched  
644 compared to Triassic evaporites and the  $\epsilon^{34}\text{S}$  is consequently very low (Fig.13 and 14). The  
645 weak sulfur isotopes fractionation between sulfides and sulfates at SMTZ have been already  
646 demonstrated for diagenetic fronts developed close to the seafloor and is the consequence of  
647 an open system for sulfate supply (Jørgensen et al., 2004; Borowski et al., 2013; Magnall et  
648 al., 2016).

649 We saw that the precipitation of Type I and Type II can happened in distinct condi-  
650 tions in terms of sulfate availability (open versus closed systems) that led to a different evolu-  
651 tion of sulfur isotopic composition for the respective barite-sulfide deposits. Type I minerali-



652 zation was clearly associated to a shallow BSR during periodical sulfate-rich water percola-  
653 tion from ephemeral playa lake occurring during the first step of the onlap of Middle Triassic  
654 sediments (Fig.14). This configuration thus provided a limited quantity of sulfate. On the con-  
655 trary, Type II mineralization reveals early burial conditions with an ore trapping in the karst  
656 controlled by the convergence of a permanent downward sulfate flux from the overlying  
657 evaporitic lake and the upward migration of deep hydrocarbon forming the SMTZ (Fig.14).  
658 Perennial supply of sulfates for the Type II mineralization, defining the “open system”, is  
659 probably governed by the seal capacity for downward fluids at the unconformity surface. In  
660 the case of Belbezet Mine and Montifort Road, the paleokarst surface is covered by thick  
661 conglomerate and sandstones respectively, both lithologies favoring the continuous percola-  
662 tion of the sulfate-rich water during the burial of the series. On the contrary, in the case of the  
663 Olmet Road, the direct sealing of the paleokarst system by a thick marly cover could explain  
664 the isolation during burial and the lack of Type II mineralization.

665

666

### 667 **5.3 Genetic model for syngeneetic to early diagenetic ore deposits**

668 The two distinct ore trapping mechanisms evidenced in this work during the Middle  
669 Triassic period of the Lodève Basin allow us to propose a conceptual model of syngeneetic  
670 to early diagenetic ore deposits. This model presents the interconnection of sedimentary  
671 basin geodynamics, meteoric karst evolution and migration of deep basinal hydrocarbon-rich  
672 fluids in the development of very shallow barite-sulfides deposits. Three main stages can be  
673 distinguished (Fig. 15):

674 (i) Stage 1: Intense weathering and epigenetic karstification after the post-rift exhumation of  
675 the basin

676 After the Permian rifting of the Lodève basin, a significant base level drop of about  
677 1500m, resulting from a general uplift of the margins during the initiation of the Tethys-  
678 Ligure basin opening (Lopez, 1992), caused the widespread erosion of the Late Permian  
679 sedimentary deposits and the differential exhumation of the Hercynian basement (Fig.15 –  
680 Stage 1). All the studied outcrops show precisely the base of the Middle Triassic pile  
681 overlapping a well define paleokarstic surface characterized by paleolapiaz, potholes and exo-  
682 and endokarstic cavity networks. At the Roche Percée ore dyke, relevant withdrawal  
683 structures and collapse fabric indicate a mechanism of karstification associated to *per*  
684 *descensum* sedimentary infilling of a major deep paleo-pothole developed along a vertical  
685 permeability barrier between the calcschists and the dolomites. Exokarstic processes prior to  
686 the deposition of Middle Triassic basal formation is also well-observed along the Olmet Road  
687 with the development of paleo-potholes and weathering markers along the Middle Triassic  
688 paleosurface. In addition, the Montifort Road outcrop reveals the strings of interconnected  
689 planar cavities which indicate endokarstic dissolution processes at the front of a fluctuating  
690 water table, prior to or just at the beginning of the deposition of the first Middle Triassic  
691 sediments. During the dissolution of the surrounding calcschists, the insoluble fraction  
692 including silt-sized quartz and iron oxides was accumulated in the cavities and conduits  
693 forming typical vadose silt deposits with granules. Such micro-nodular pedogenic granules  
694 were also described in the Late Cretaceous-Early Tertiary of the southern France by Plaziat  
695 and Freytet (1978) with possible reverse grading reported to the development of pseudo-  
696 microkarst (Freytet and Plaziat, 1978, 1982; Hay and Wiggins, 1980; Alonso-Zarza, 2003). In  
697 this case overlapping of pedogenic, vadose and shallow phreatic processes led to the

698 granification of sediments (Mazzullo and Birdwell, 1989) controlled by periodical changes in  
699 the position of the water table (Alonso-Zarza, 2003). This stage corresponds to the formation  
700 of the karst trap for later mineralizations.

701

702 *(ii) Stage 2: Alkaline stage during the playa lake initiation*

703         The silicification strengthening the walls of the Roche Percée ore dyke occurred  
704 before the main karstic infilling, partially plugging the karstic paleosurface of Montifort Road  
705 and Belbezet Mine (Fig.15 – Stage 2). Silica came from the partial leaching of the quartz silt-  
706 fraction dispersed in the basement from the exokarst to the drowned endokarst network. In the  
707 surficial domain, the abundance of chalcedony filling the fracture network is compatible with  
708 Group III silcrete pedogenesis of arid-alkaline environments as defined by Summerfield  
709 (1983a, 1983b) and Wopfner (1983). In the endokarst, the alkaline tendency probably favored  
710 silt-size quartz partial leaching. Periodical mixing with low acid rainwaters led to the growth  
711 of drusy quartz in the residual intergranular space and to partial silicification of the  
712 intrakarstic sediments (Nash and Ulliyott, 2007; Ulliyott and Nash, 2016).

713

714 *(iii) Stage 3: Early diagenetic ore deposition during the permanent evaporitic lake deposi-*  
715 *tional system*

716         The karst reservoir was then subjected to two ore trapping stages during the  
717 progressive emplacement by the permanent sulfate-rich lake system: a synsedimentary event  
718 (Stage 3A) and an early burial process (Stage 3B) (Fig.15 – Stage 3).

719         *Stage 3A – Type I mineralization:* the karst sedimentary infilling was composed of  
720 detrital-chemical depositional cycles compatible with humid-arid climate alternations and  
721 emplacement of shallow sulfate-rich lake (Lopez and Mader, 1985). During humid periods,

722 part of the fine grained fraction derived from the weathering processes on the flanks of the  
723 paleo-highs was mobilized by the running waters and transported from exokarst systems  
724 toward the endokarstic cavities to form vadose silts and sands deposition. During the dry  
725 season, the lake depositional system was submitted to intense evaporation and evaporite  
726 precipitation. Part of the sulfate-rich waters and evaporite crystals were dragged toward the  
727 exokarst systems to give cyclic chemical laminae. At the same time, the presence of organic  
728 matter-rich material within karstic cavities favored the bacterial reduction of the downward  
729 percolating sulfates in the karst network. The source of metals probably derived from the  
730 meteoric leaching of outcropping previous MVT ore deposits from the paleoreliefs upstream  
731 the karst trap. Therefore, Type I mineralization clearly conjugated a synsedimentary gravity-  
732 driven mineralized brine with a BSR process that interacted in the meteoric karst network.

733         *Stage 3B – Type II mineralization:* during the early burial of the karst systems, the seal  
734 capacity of the Middle Triassic marls led to the trapping of the ascending hydrocarbon-rich  
735 fluids below this permeability barrier. Permanent downward sulfate-rich water still continued  
736 to percolate into the buried karst where permeable coarse material locally overlapped the  
737 paleosurface. The interaction between ascending hydrocarbon and the BSR zone formed a  
738 SMTZ which represented the upper chemical boundary for an underlying zone undersaturated  
739 in sulfates that led to the dissolution of previous buried Permian barite-rich ore deposits.  
740 Released barium, metals and sulfur were transported by the *per ascensum* reducing brine  
741 containing the hydrocarbon. During the ascension through the sedimentary pile, this solution  
742 reached the SMTZ window where dissolved sulfates were available. The increase of alkalinity  
743 was first responsible for the precipitation of ankerite on the walls of the cavities, closely  
744 associated with hydrocarbons markers. Barite and sulfides then precipitated, thus plugging the  
745 cavities to form the Type II mineralizations.

746

747

## 748 **6. Conclusions**

749         The originality of this work lies in the multi-scale analysis of an exceptional field  
750 example of continental diagenetic barite-sulfide deposits precipitated within meteoric karst  
751 systems. Ore deposits have been the subject of sedimentological and texture analysis, sulfur  
752 and strontium isotopes and fluid inclusions microthermometry. This methodology allows us to  
753 propose a genetic model of synsedimentary to early diagenetic metallogenesis in which we  
754 constrained all the factors whose interactions over time formed a favorable metallogenic: karst  
755 dynamics, chemistry of the water table linked to climate and depositional environment  
756 changes, location of thermogenic hydrocarbons dysmigrations and the remobilization of  
757 former polymetallic deposits.

758 Four keypoints can be retained from this study:

- 759         • The importance of the interaction between the evolution of meteoric karsts during  
760 climate changes and the location of ore deposits. Epigene karstification plays both a  
761 fundamental precursor role, guiding the path of mineralizing fluids and constituting  
762 the main trap, and a passive role by undergoing the precipitation of the fluids which  
763 will then stop the karst evolution at the origin of mineralized paleokarsts.
- 764         • The predominant control of climate fluctuations, depositional environment changes  
765 and redox conditions at the water table on timing and texture of shallow continental  
766 diagenetic ore deposits. We show that the progressive transition from ephemeral playa  
767 lake to perennial evaporitic lake environments controls the supply of sulfates for min-  
768 eralization and the position of the SMTZ by the interaction with ascending hydrocar-  
769 bons.

770

771 • The significant impact of the thermogenic hydrocarbon migration in the metallogeny  
772 of sedimentary basins: passive role in the development of MVT ore deposits since the  
773 location of oil traps are constrained by the early mineralizations, and a foreground role  
774 in the supergene metallogeny by constituting a main vector in the redistribution of  
775 metals few meters below the SWI.

776 • The superimposition in a single trap of two very similar syngene to early dia-  
777 genetic mineralizations but implying different origins of fluids (surficial versus deep  
778 basinal brines) during the first step of burial along a karstic surface (notion of “*sliding*  
779 *metallogenic window effect*”).

780 **Acknowledgments**

781 We are grateful to Total Company (France) who funded all the field and laboratory  
782 works during the thesis. We wish to thank Christophe Nevado and Doriane Delmas of  
783 the Thin Section Lab at University of Montpellier for their work of high quality  
784 which represented a solid foundation for this study. We also thank Bernard Boyer  
785 and Claude Merlet at CNRS-University of Montpellier (France) for their technical  
786 support with sulfur isotopes measurements on SIMS, and Olivier Bruguier for his  
787 help in the strontium concentration analyses on LA-ICPMS at Géosciences Montpel-  
788 lier. Finally, the Editor Sadoon Morad and the two reviewers are thanked for  
789 thoughtful and constructive reviews which greatly improved the manuscript.

790 **Figures captions**

791

792 **Figure 1:** Geological setting of the Lodève Permian basin. A) Simplified geological map. The  
793 black square indicates the location of the detailed geological map of the study area illustrated  
794 in Fig.2A. B) North-south cross section of the Lodève half-graben. The location of the cross  
795 section is indicated by the North-South bold line A-A' on Fig.1A.

796

797 **Figure 2:** A) Detailed geological map of the study area (see Fig.1A for the location). All the  
798 studied outcrops are designated by a star and a letter, from a to j, that refers to the Appendix A.  
799 B) SW-NE cross-section of the study area (the location is marked by a dashed line on Fig.2A).  
800 C) Sedimentological log of the Triassic series above the post-rift unconformity of the Lodève  
801 Basin.

802

803 **Figure 3:** The Roche Percée paleo-pothole. A) Geological map of the site. B) General  
804 architecture of the paleokarst infill with the west side at left (View 1) and southern side at  
805 right (View 2). C) Detailed views of the intrakarstic infilling with the section a (left) and  
806 section b (right) located on the Fig.3A.

807

808 **Figure 4:** Close-up photos and photomicrographs of the Roche Percée paleo-pothole infill. A)  
809 Successive breccia packages (c) bordered by the silicified calcschists (a) and including  
810 collapsed silicified blocks (b) and gypsum-anhydrite boxworks (white arrows). B) Close-up  
811 view of RP2 Facies showing millimetre-thick massive barite layers (white arrow) and nodules  
812 (b) alternating with laminated dolomite-rich siltstone. C) Thin section of graded beds of the  
813 RP2 Facies (plain-polarized light-PPL). D) Detailed view of a barite crystallite of the previous  
814 thin section (C) showing clear corroded (yellow arrows) and broken surfaces (yellow circle)  
815 (PPL). E. Photomicrograph of chalcopyrites crystallized within barite mineralization  
816 (reflected light-RL).

817

818 **Figure 5:** General architecture of the Olmet Road paleo-lapiaz. A) Interpreted drawing of the  
819 outcrop. B) Photo of the western part of the outcrop (see A for location) (tm: Triassic marls;  
820 sd: sulfides-rich fine sandstones; ba: barite pockets; ib: sulfide impregnated bands and  
821 fractures; cd: Cambrian dolomites. C) Photo of the central part of the outcrop (see A for



822 location) showing the main fault-damaged zone and barite-sulfide mineralizations in both  
823 hanging wall and footwall of the fault (cd: Cambrian dolomites; ba: barite; fb: tectonic breccia;  
824 ls: laminated sulfides-rich silty claystone; sd: sulfide-rich sandstone to siltstone; tm: Triassic  
825 marls).

826

827 **Figure 6:** Architecture and mineralized facies of the Montifort Road planar cavities string. A)  
828 General view and line-drawing of the outcrop showing the sub-planar endokarstic cavity  
829 cluster crossing the Cambrian calcschists. B) Close-up drawing of the southern part of the  
830 outcrop (see on A) with a detailed view of a planar cavity. C) Polished hand-sample section of  
831 a karstic cavity infill (ba: barite; gr: reverse graded granules; sic: silicification; black arrows:  
832 ankerite).

833

834 **Figure 7:** A) Photomicrographs of the base of figure 6C showing the intrakarstic sediments in  
835 the mineralized cavities of Montifort Road (an/white arrows: ankerite; gr: iron-rich silty  
836 dolomudstone grains; dq: drusy quartz; vs: geopetal silt infill) (Left PPL, Right cross-  
837 polarized light-XPL). B) Drusy ankerites growing on the phreatic drusy megaquartz (PPL). C)  
838 Contact zone between drusy ankerite and large barite slats (PPL). D) Photomicrograph in  
839 fluorescence X showing organic matter patches at the contact between drusy ankerite and host  
840 rock, and within barite mineralization. E) Scanning Electron Microscope (SEM) image  
841 illustrating numerous euhedral pyrites close to the contact between barite and late sparitic  
842 calcite.

843

844 **Figure 8:** General fabric of the Belbezet mine paleo-potholes and endokarst. A) Drawing of  
845 the main gallery close to the entrance showing the architecture of the ore deposit. B) Detail  
846 photo of the south-western face (see A for location) showing the Cambrian dolomites (cd)  
847 grooved by decimetre to meter-deep potholes (white dotted line) and filled by sulfide/barite-  
848 rich silty deposits (sb) reworked on top by bitumen-rich sulfide-barite deposits (rsb). C) Detail  
849 photo of bitumen-rich barite mineralization cementing a block of Cambrian dolomite (circled  
850 pencil is 15cm) (same legend than before). D) Close-up photo showing bitumen blebs (bi) and  
851 partly weathered grey copper sulfides (cs) cementing the white barite breccia.

852

853 **Figure 9:** Photomicrographs of primary fluid inclusions trapped within barite (PPL). A)  
854 Single-phase (1-phase FI) and two-phase (2-phase FI) inclusions in the barite (ba) sealing the  
855 endokarstic network of the Montifort Road outcrop. B) Essentially single-phase liquid  
856 inclusions (1-phase FI) entrapped within the barite of the Roche Percée paleo-pothole.  
857

858 **Figure 10:** Histograms showing microthermometric  $T_e$ ,  $T_{mIce}$  and  $T_h$  data obtained for  
859 primary two-phase fluid inclusions entrapped within barite crystals of the Montifort Road  
860 outcrop corresponding to the mineralized infill of the planar cavities string (MR1 Facies) and  
861 barite precipitated within veins affected the Cambrian dolomites (MR2 Facies).  
862

863 **Figure 11:** Synthetic paragenetic sequence and associated fabric for the post-rift Middle  
864 Triassic intrakarstic ore deposits.  
865

866 **Figure 12:** Graph of  $^{87}Sr/^{86}Sr$  vs Sr concentration (in ppm) of Middle Triassic post-rift barites  
867 belonging to the MR1, BM and RP2 Facies and the three distinct Late Permian syn-rift  
868 mineralizing events (described in Laurent et al., 2017). The range of strontium isotopic  
869 composition of the Triassic evaporites is reported from Koepnick et al. (1990) and Song et al.  
870 (2015). Analytical errors is  $\pm 0.000010$  for  $^{87}Sr/^{86}Sr$  in barites.  
871

872  
873 **Figure 13:**  $\delta^{34}S$  diagram illustrating the signatures of the Triassic evaporites (grey star for  
874 gypsum and hexagon for anhydrite), barites (white circles) and chalcopyrites (black rectangle  
875 with error bars) of the Middle Triassic mineralizations (Type I and Type II) and Late Permian  
876 MVT ore deposits (Laurent et al., 2017). Analytical errors are  $\pm 0.2\%$  for  $\delta^{34}S$  in barites and  
877 Triassic evaporites, and  $\pm 1\%$  for  $\delta^{34}S$  in chalcopyrites.  
878

879 **Figure 14:**  $\delta^{34}S$ -depth diagram showing the partitioning of barites and chalcopyrites for the  
880 Type I and Type II Middle Triassic ore deposits compared to the Triassic evaporites signature.  
881 The calculated  $\epsilon^{34}S$  ( $= \delta^{34}S_{barite} - \delta^{34}S_{chalcopyrite}$ ) is also indicated for each fronts (left figure).  
882 The mineralized front migrated upward during the progressive onlap and base level rise along  
883 the karstified paleosurface as a sliding biochemical window (right figure).  
884

885 **Figure 15:** Conceptual model of the syndimentary to early diagenetic ore deposition  
886 following the post-rift exhumation of the Lodève Basin's northern margin: Stage 1 –  
887 Exhumation, intense weathering and epigene karstification with vadose sediment infill; Stage  
888 2 – Initial alkaline playa lake development, quartz leaching and vadose-phreatic silicifications  
889 during an increase of acidification; and Stage 3 – Perennial sulfate-rich lake development and  
890 syndimentary to early diagenetic barite-sulfide trapping (Type I and Type II  
891 mineralizations).

892

893 **Table 1:** Fluid inclusion petrography and microthermometry data (Te, TmIce, Th and salinity)  
894 for the barites of the Middle Triassic ore deposits.

895

896 **Table 2:**  $^{87}\text{Sr}/^{86}\text{Sr}$  and strontium concentration for barites and  $\delta^{34}\text{S}$  for barites and  
897 synchronous chalcopyrites in the ore facies of the different studied area in this paper and for  
898 the three Late Permian MVT ore events presented in Laurent et al. (2017). Analytical errors  
899 are  $\pm 0.2\text{‰}$  for  $\delta^{34}\text{S}$  in barites and Triassic evaporites,  $\pm 1\text{‰}$  for  $\delta^{34}\text{S}$  in chalcopyrites and  
900  $\pm 0.000010$  for  $^{87}\text{Sr}/^{86}\text{Sr}$  in barites.

901

902 **Appendix A:** Location and ore characteristics (architecture, mineralogy and classification) of  
903 the 10 sites studied in this entire work. Only 4 sites (in bold letters) have been chosen for a  
904 detailed description in this paper: Montifort Road, Roche Percée, Belbezet Mine and Olmet  
905 Road. The small letters refer to the map in Fig.2A.

906

907 **Bibliography**

908

909 Aloisi, G., Pierre, C., Rouchy, J.-M., Foucher, J.-P., Woodside, J., others, 2000. Methane-  
910 related authigenic carbonates of eastern Mediterranean Sea mud volcanoes and their  
911 possible relation to gas hydrate destabilisation. *Earth Planet. Sci. Lett.* 184, 321–338.

912 Aloisi, G., Wallmann, K., Bollwerk, S.M., Derkachev, A., Bohrmann, G., Suess, E., 2004.  
913 The effect of dissolved barium on biogeochemical processes at cold seeps. *Geochim.*  
914 *Cosmochim. Acta* 68, 1735–1748.

915 Alonso-Zarza, A. M. (2003). Palaeoenvironmental significance of palustrine carbonates and  
916 calcretes in the geological record. *Earth-Science Reviews*, 60(3-4), 261-298.

917 Alperin, M. J., Reeburgh, W. S., Whiticar, M. J., 1988. Carbon and hydrogen isotope  
918 fractionation resulting from anaerobic methane oxidation. *Global biogeochemical cycles*,  
919 2(3), 279-288.

920 Aquilina, L., Dia, A.N., Boulègue, J., Bourgois, J., Fouillac, A.M., 1997. Massive barite  
921 deposits in the convergent margin off Peru: Implications for fluid circulation within  
922 subduction zones. *Geochim. Cosmochim. Acta* 61, 1233–1245.

923 Arndt, S., Brumsack, H.-J., Wirtz, K.W., 2006. Cretaceous black shales as active bioreactors:  
924 a biogeochemical model for the deep biosphere encountered during ODP Leg 207  
925 (Demerara Rise). *Geochim. Cosmochim. Acta* 70, 408–425.

926 Arning, E.T., Gaucher, E.C., van Berk, W., Schulz, H.-M., 2015. Hydrogeochemical models  
927 locating sulfate-methane transition zone in marine sediments overlying black shales: A  
928 new tool to locate biogenic methane? *Mar. Pet. Geol.* 59, 563–574.

929 Barnes, R.O., Goldberg, E.D., 1976. Methane production and consumption in anoxic marine  
930 sediments. *Geology* 4, 297–300.

931 Bodnar, R., 1994. Synthetic fluid inclusions: XII. The system H<sub>2</sub>O-NaCl. Experimental  
932 determination of the halite liquidus and isochores for a 40 wt% NaCl solution. *Geochim.*  
933 *Cosmochim. Acta* 58, 1053–1063. [https://doi.org/10.1016/0016-7037\(94\)90571-1](https://doi.org/10.1016/0016-7037(94)90571-1)

934 Bodnar, R.J., 1993. Revised equation and table for determining the freezing point depression  
935 of H<sub>2</sub>O-NaCl solutions. *Geochim. Cosmochim. Acta*; (United States) 57.

- 936 Bodnar, R.J., 1985. Fluid inclusion systematics in epithermal systems. *Rev. Econ. Geol.* 2,  
937 73–97.
- 938 Borisenko, A.S., 1977. Study of the salt composition of solutions in gas-liquid inclusions in  
939 minerals by the cryometric method. *Sov. Geol. Geophys.* 18, 11-18.
- 940 Borowski, W.S., Rodriguez, N.M., Paull, C.K., Ussler, W., 2013. Are <sup>34</sup>S-enriched authigenic  
941 sulfide minerals a proxy for elevated methane flux and gas hydrates in the geologic  
942 record? *Mar. Pet. Geol.* 43, 381–395. <https://doi.org/10.1016/j.marpetgeo.2012.12.009>
- 943 Borowski, W.S., Paull, C.K., Ussler, W., 1999. Global and local variations of interstitial  
944 sulfate gradients in deep-water, continental margin sediments: Sensitivity to underlying  
945 methane and gas hydrates. *Mar. Geol.* 159, 131–154.
- 946 Borowski, W.S., Paull, C.K., Ussler, W., 1997. Carbon cycling within the upper  
947 methanogenic zone of continental rise sediments; an example from the methane-rich  
948 sediments overlying the Blake Ridge gas hydrate deposits. *Mar. Chem.* 57, 299–311.
- 949 Br  h  ret, J.-G., Brumsack, H.-J., 2000. Barite concretions as evidence of pauses in  
950 sedimentation in the Marnes Bleues Formation of the Vocontian Basin (SE France).  
951 *Sediment. Geol.* 130, 205–228.
- 952 Brown, P.E., 1989. FLINCOR; a microcomputer program for the reduction and investigation  
953 of fluid-inclusion data. *Am. Mineral.* 74, 1390–1393.
- 954 Brown, P.E., Lamb, W.M., 1989. P-V-T properties of fluids in the system H<sub>2</sub>O±CO<sub>2</sub>±NaCl:  
955 New graphical presentations and implications for fluid inclusion studies. *Geochim.*  
956 *Cosmochim. Acta* 53, 1209–1221.
- 957 Brumsack, H.J., 1986. The inorganic geochemistry of Cretaceous black shales (DSDP Leg 41)  
958 in comparison to modern upwelling sediments from the Gulf of California. *Geol. Soc.*  
959 *London, Spec. Publ.* 21, 447–462.
- 960 Canfield, D.E., 2001. Biogeochemistry of sulfur isotopes. *Rev. Mineral. Geochemistry* 43,  
961 607–636.
- 962 Cohen, A. I., Gordon, L., 1961. Co-precipitation in some binary sulphate systems. *Talanta*,  
963 7(3-4), 195-211.

- 964 Crawford, M.L., 1981. Phase equilibria in aqueous fluid inclusions. Short course fluid  
965 inclusions. *Appl. Petrol* 6, 75-100.
- 966 Dickens, G.R., 2001. Sulfate profiles and barium fronts in sediment on the Blake Ridge:  
967 present and past methane fluxes through a large gas hydrate reservoir. *Geochim.*  
968 *Cosmochim. Acta* 65, 529–543.
- 969 Duan, Z., Møller, N., Weare, J.H., 1992. An equation of state for the CH<sub>4</sub>-CO<sub>2</sub>-H<sub>2</sub>O system: I.  
970 Pure systems from 0 to 1000°C and 0 to 8000 bar. *Geochim. Cosmochim. Acta* 56,  
971 2605–2617. [https://doi.org/10.1016/0016-7037\(92\)90347-L](https://doi.org/10.1016/0016-7037(92)90347-L)
- 972 Echtler, H., Malavieille, J., 1990. Extensional tectonics, basement uplift and Stephano-  
973 Permian collapse basin in a late Variscan metamorphic core complex (Montagne Noire,  
974 Southern Massif Central). *Tectonophysics* 177, 125–138. [https://doi.org/10.1016/0040-  
975 1951\(90\)90277-F](https://doi.org/10.1016/0040-1951(90)90277-F)
- 976 Fernandes, N.A., Gleeson, S.A., Magnall, J.M., Creaser, R.A., Martel, E., Fischer, B.J., Sharp,  
977 R., 2017. The origin of Late Devonian (Frasnian) stratiform and stratabound mudstone-  
978 hosted barite in the Selwyn Basin, Northwest Territories, Canada. *Mar. Pet. Geol.* 85, 1–  
979 15. <https://doi.org/10.1016/j.marpetgeo.2017.04.006>
- 980 Freytet, P., & Plaziat, J. C., 1982. Continental carbonate sedimentation and pedogenesis-Late  
981 Cretaceous and Early Tertiary of southern France. *Contributions to Sedimentary Geology*,  
982 12, 213p.
- 983 Freytet, P., Plaziat, J.C., 1979. Les ooides calcaires continentaux: Diversité des formes, des  
984 gisements, des modes de formation. *Rech. Géographiques Astrasbg.* 12, 69–80.
- 985 Gand, G., Lapeyrie, J., Garric, J., Nel, A., Schneider, J., Walter, H., 1997. Découverte  
986 d'arthropodes et de bivalves inédits dans le Permien continental (Lodévois, France).  
987 *Comptes Rendus l'Académie des Sci. IIA-Earth Planet. Sci.* 325, 891–898.
- 988 Goldberg, E.D., Arrhenius, G.O.S., 1958. Chemistry of Pacific pelagic sediments. *Geochim.*  
989 *Cosmochim. Acta* 13, 153–212.
- 990 Goldstein, R.H., Reynolds, T.J., 1994. Systematics of fluid inclusions in diagenetic minerals,  
991 SEPM short course ; SEPM, Tulsa, Okla.

- 992 Gordon, L., Reimer, C. C., Burt, B. P., 1954. Distribution of strontium within barium sulfate  
993 precipitated from homogeneous solution. *Analytical Chemistry*, 26(5), 842-846.
- 994 Günther, D., Heinrich, C.A., 1999. Enhanced sensitivity in laser ablation-ICP mass  
995 spectrometry using helium-argon mixtures as aerosol carrier. *J. Anal. At. Spectrom.* 14,  
996 1363–1368.
- 997 Harrison, A.G., Thode, H.G., 1958. Mechanism of the bacterial reduction of sulphate from  
998 isotope fractionation studies. *Trans. Faraday Soc.* 54, 84–92.
- 999 Hay, R.L., Wiggins, B., 1980. Pellets, ooids, sepiolite and silica in three calcretes of the  
1000 southwestern United States. *Sedimentology* 27, 559–576.
- 1001 Hoehler, T. M., Alperin, M. J., Albert, D. B., Martens, C. S., 1994. Field and laboratory  
1002 studies of methane oxidation in an anoxic marine sediment: Evidence for a  
1003 methanogen-sulfate reducer consortium. *Global Biogeochemical Cycles*, 8(4), 451-463.
- 1004 Hu, C.Y., Frank Yang, T., Burr, G.S., Chuang, P.C., Chen, H.W., Walia, M., Chen, N.C.,  
1005 Huang, Y.C., Lin, S., Wang, Y., Chung, S.H., Huang, C. Da, Chen, C.H., 2017.  
1006 Biogeochemical cycles at the sulfate-methane transition zone (SMTZ) and geochemical  
1007 characteristics of the pore fluids offshore southwestern Taiwan. *J. Asian Earth Sci.* 149,  
1008 172–183. <https://doi.org/10.1016/j.jseaes.2017.07.002>
- 1009 Jørgensen, B.B., Böttcher, M.E., Lüschen, H., Neretin, L.N., Volkov, I.I., 2004. Anaerobic  
1010 methane oxidation and a deep H<sub>2</sub>S sink generate isotopically heavy sulfides in Black Sea  
1011 sediments. *Geochim. Cosmochim. Acta* 68, 2095–2118.
- 1012 Kastner, M., Elderfield, H., Martin, J.B., Suess, E., Kvenvolden, K.A., Garrison, R.E., 1990.  
1013 Diagenesis and interstitial-water chemistry at the Peruvian continental margin—major  
1014 constituents and strontium isotopes, in: Suess, E., von Huene, R., et Al., *Proc. ODP, Sci.*  
1015 *Results*, 413–440.
- 1016 Knittel, K., Boetius, A., 2009. Anaerobic oxidation of methane: progress with an unknown  
1017 process. *Annu. Rev. Microbiol.* 63, 311–334.
- 1018 Koepnick, R.B., Denison, R.E., Burke, W.H., Hetherington, E.A., Dahl, D.A., 1990.  
1019 Construction of the Triassic and Jurassic portion of the Phanerozoic curve of seawater  
1020 <sup>87</sup>Sr/<sup>86</sup>Sr. *Chem. Geol. Isot. Geosci. Sect.* 80, 327–349.

- 1021 Laurent, D., 2015. Marqueurs de la dynamique des fluides associée à l'enfouissement des  
1022 bassins sédimentaires : Exemples du Bassin Permien de Lodève (France) et du North  
1023 Viking Graben (Mer du Nord). Doctoral dissertation, Université de Montpellier, 622p.
- 1024 Laurent, D., Lopez, M., Chauvet, A., Sauvage, A.C., Buatier, M., Spangenberg, J.E., 2017.  
1025 Sedimentary fluids/fault interaction during syn-rift burial of the Lodève Permian Basin  
1026 (Hérault, France): An example of seismic-valve mechanism in active extensional faults.  
1027 *Mar. Pet. Geol.* 88, 303–328. <https://doi.org/10.1016/j.marpetgeo.2017.08.021>
- 1028 Leach, D.L., Taylor, R.D., Fey, D.L., Diehl, S.F., Saltus, R.W., 2010. A deposit model for  
1029 Mississippi Valley-Type lead-zinc ores. *Miner. Depos. Model. Resour. Assess.*
- 1030 Lerouge, C., Grangeon, S., Gaucher, E.C., Tournassat, C., Agrinier, P., Guerrot, C., Widory,  
1031 D., Fléhoc, C., Wille, G., Ramboz, C., Vinsot, A., Buschaert, S., 2011. Mineralogical  
1032 and isotopic record of biotic and abiotic diagenesis of the Callovian-Oxfordian clayey  
1033 formation of Bure (France). *Geochim. Cosmochim. Acta* 75, 2633–2663.  
1034 <https://doi.org/10.1016/j.gca.2011.02.025>
- 1035 Lopez, M., 1993. The Lodève Permian Basin. Post-Conference fieldtrip, in: *Geofluids'93*.  
1036 Torquay, 190p.
- 1037 Lopez, M., 1992. Dynamique du passage d'un appareil terrigène à une plate-forme carbonatée  
1038 en domaine semi-aride le Trias de Lodève, sud de la France. Doctoral dissertation,  
1039 Université des Sciences et Techniques du Languedoc, Montpellier.
- 1040 Lopez, M., Gand, G., Garric, J., Körner, F., Schneider, J., 2008. The playa environments of  
1041 the Lodève Permian basin (Languedoc-France). *J. Iber. Geol.* 34, 29–56.
- 1042 Lopez, M., Mader, D., 1985. Gravelly and sandy braidplain evolving into floodplain and  
1043 playa lake deposits and vice versa in the Buntsandstein-facies sediments and marine  
1044 incursions in the Triassic of the Lodève region (Southern France). In *Aspects of Fluvial*  
1045 *Sedimentation in the Lower Triassic Buntsandstein of Europe*. Springer, Berlin,  
1046 Heidelberg, 509-518.
- 1047 Lopez, M., Mader, D., 1992. Palaeoecological and palaeoenvironmental evolution of Permian  
1048 and Triassic fluvial basins in Europe, Buntsandstein and Keuper Facies. Gustav Fischer  
1049 Verlag publisher.



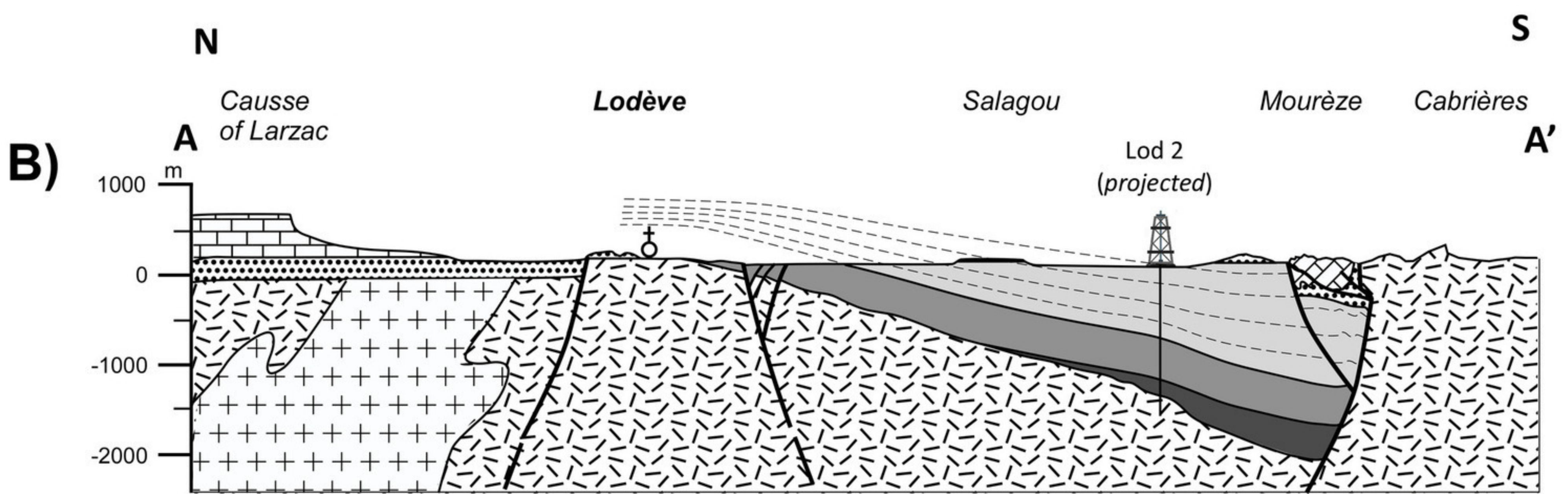
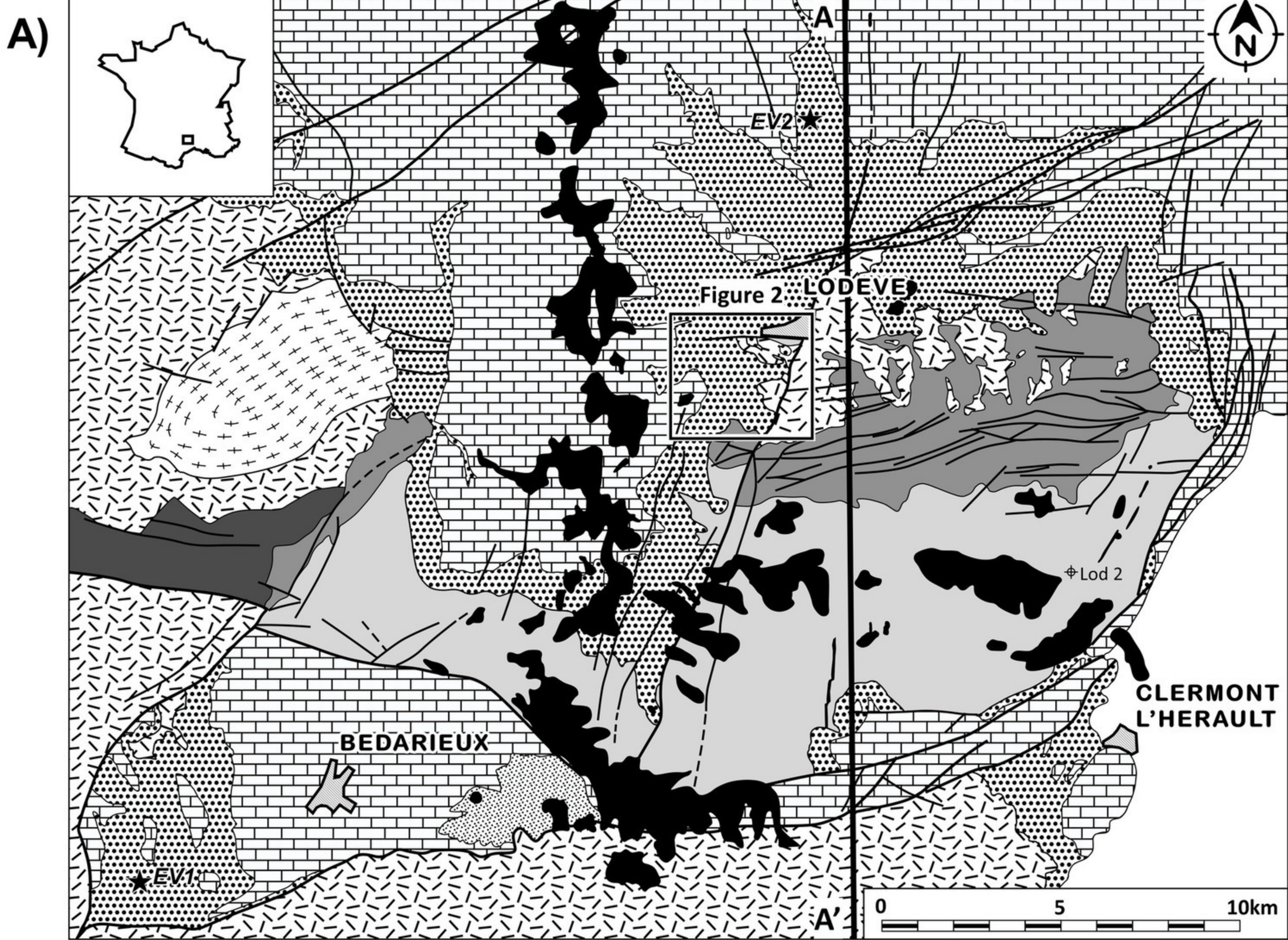
- 1050 Lopez, M., Petit, J.P., 2003. Outcrop analogues for Carboniferous and Rotliegende Dutch  
1051 Oilfields in the Lodève Permian Basin, South of France. Fieldtrip Guid. inédit, Lab. Dyn.  
1052 la Lithosphère, Montpellier II.
- 1053 Machel, H.G., Krouse, H.R., Sassen, R., 1995. Products and distinguishing criteria of  
1054 bacterial and thermochemical sulfate reduction. *Appl. geochemistry* 10, 373–389.
- 1055 Machel, H.G., 2001. Bacterial and thermochemical sulfate reduction in diagenetic settings –  
1056 old and new insights. *Sediment. Geol.* 140, 143-175.
- 1057 Magnall, J.M., Gleeson, S.A., Stern, R.A., Newton, R.J., Poulton, S.W., Paradis, S., 2016.  
1058 Open system sulphate reduction in a diagenetic environment - Isotopic analysis of barite  
1059 ( $\delta^{34}\text{S}$  and  $\delta^{18}\text{O}$ ) and pyrite ( $\delta^{34}\text{S}$ ) from the Tom and Jason Late Devonian Zn-Pb-Ba  
1060 deposits, Selwyn Basin, Canada. *Geochim. Cosmochim. Acta* 180, 146–163.  
1061 <https://doi.org/10.1016/j.gca.2016.02.015>
- 1062 Matter, A., Peters, T., Ramseyer, K., 1987.  $^{87}\text{Sr}/^{86}\text{Sr}$ -Verhältnisse und Sr-Gehalte von  
1063 Tiefengrundwässern, Mineralien sowie Gesteinen aus dem Kristallin und der Trias der  
1064 Nordschweiz. *Eclogae Geol. Helv.* 80, 579–592.
- 1065 Mazzullo, S. J., Birdwell, B. A., 1989. Syngenetic formation of grainstones and pisolites from  
1066 fenestral carbonates in peritidal settings. *Journal of Sedimentary Research*, 59(4), 605-  
1067 611.
- 1068 Meister, P., Mckenzie, J.A., Vasconcelos, C., Bernasconi, S., Frank, M., Gutjahr, M., Schrag,  
1069 D.P., 2007. Dolomite formation in the dynamic deep biosphere: results from the Peru  
1070 Margin. *Sedimentology* 54, 1007–1032.
- 1071 Moore, T.S., Murray, R.W., Kurtz, A.C., Schrag, D.P., 2004. Anaerobic methane oxidation  
1072 and the formation of dolomite. *Earth Planet. Sci. Lett.* 229, 141–154.
- 1073 Nash, D.J., Ullyott, J.S., 2007. Silcrete. *Geochemical sediments and landscapes* 95–148.
- 1074 Niemann, H., Duarte, J., Hensen, C., Omoregie, E., Magalhaes, V.H., Elvert, M., Pinheiro,  
1075 L.M., Kopf, A., Boetius, A., 2006. Microbial methane turnover at mud volcanoes of the  
1076 Gulf of Cadiz. *Geochim. Cosmochim. Acta* 70, 5336–5355.

- 1077 Odin, B., 1986. Les formations permienes, Autunien supérieur à Thuringien, du “bassin” de  
1078 Lodève (Hérault, France) stratigraphie, minéralogie, paléoenvironnements, corrélations.  
1079 Doctoral dissertation, Université d'Aix-Marseille, p. 375.
- 1080 Ohmoto, H., 1990. Systematics of sulphur isotopes in recent marine sediments and ancient  
1081 sediment-hosted base metal deposits. *Stable Isot. fluid Process. Miner.* 23, 70–120.
- 1082 Ohmoto, H., Lasaga, A.C., 1982. Kinetics of reactions between aqueous sulfates and sulfides  
1083 in hydrothermal systems. *Geochim. Cosmochim. Acta* 46, 1727–1745.
- 1084 Pin, C., Bassin, C., 1992. Evaluation of a strontium-specific extraction chromatographic  
1085 method for isotopic analysis in geological materials. *Anal. Chim. Acta* 269, 249–255.
- 1086 Plaziat, J. C., Freytet, P., 1978. Le pseudo-microkarst pédologique: un aspect particulier des  
1087 paléo-pédogenèses développées sur les dépôts calcaires lacustres dans le Tertiaire du  
1088 Languedoc. *Comptes Rendues Academie Science Paris*, 286, 1661-1664.
- 1089 Postgate, J.R., Schwartz, W., 1985. *The Sulfate-Reducing Bacteria* (2nd Edition). *J. Basic*  
1090 *Microbiol.* 25, 202. <https://doi.org/10.1002/jobm.3620250311>
- 1091 Raiswell, R., Fisher, Q.J., 2004. Rates of carbonate cementation associated with sulphate  
1092 reduction in DSDP/ODP sediments: implications for the formation of concretions. *Chem.*  
1093 *Geol.* 211, 71–85.
- 1094 Reeburgh, W.S., 1983. Rates of biogeochemical processes in anoxic sediments. *Annu. Rev.*  
1095 *Earth Planet. Sci.* 11, 269–298.
- 1096 Reeburgh, W.S., 1976. Methane consumption in Cariaco Trench waters and sediments. *Earth*  
1097 *Planet. Sci. Lett.* 28, 337–344.
- 1098 Renault, J., Brower, E., 1971. X-ray line broadening in the barium sulfate-strontium sulfate  
1099 series. *American Mineralogist: Journal of Earth and Planetary Materials*, 56(7-8), 1481-  
1100 1485.
- 1101 Riedinger, N., Kasten, S., Gröger, J., Franke, C., Pfeifer, K., 2006. Active and buried  
1102 authigenic barite fronts in sediments from the Eastern Cape Basin. *Earth Planet. Sci. Lett.*  
1103 241, 876–887.
- 1104 Rodriguez, N.M., Paull, C.K., Borowski, W.S., 2000. Zonation of authigenic carbonates  
1105 within gas hydrate-bearing sedimentary sections on the Blake Ridge: offshore

- 1106 southeastern north America 1, in: Proceedings of the Ocean Drilling Program. Scientific  
1107 Results, 301–312.
- 1108 Roedder, E., 1984. Fluid inclusion. *Rev. Mineral.* 12, 1–394.
- 1109 Routhier, P., 1980. Où sont les métaux pour l’avenir?: les provinces métalliques: essai  
1110 demétallogénie globale. Editions du BRGM.
- 1111 Rye, R. O., Ohmoto, H., 1974. Sulfur and carbon isotopes and ore genesis: a review.  
1112 *Economic Geology*, 69(6), 826-842.
- 1113 Snyder, G.T., Dickens, G.R., Castellini, D.G., 2007. Labile barite contents and dissolved  
1114 barium concentrations on Blake Ridge: new perspectives on barium cycling above gas  
1115 hydrate systems. *J. Geochemical Explor.* 95, 48–65.
- 1116 Song, H., Wignall, P.B., Tong, J., Song, H., Chen, J., Chu, D., Tian, L., Luo, M., Zong, K.,  
1117 Chen, Y., Lai, X., Zhang, K., Wang, H., 2015. Integrated Sr isotope variations and global  
1118 environmental changes through the Late Permian to early Late Triassic. *Earth Planet. Sci.*  
1119 *Lett.* 424, 140–147. <https://doi.org/10.1016/j.epsl.2015.05.035>
- 1120 Spangenberg J.E., Lavrić J., Meisser N., Serneels V., 2010. Sulfur isotope analysis  
1121 of cinnabar from Roman wall paintings by EA/IRMS –tracking the origin of  
1122 archaeological red pigments and their authenticity. *Rapid Communications in Mass*  
1123 *Spectrometry*, 24, 2812-2816.
- 1124 Sterner, S. M., Bodnar, R. J., 1984. Synthetic fluid inclusions in natural quartz I.  
1125 Compositional types synthesized and applications to experimental geochemistry.  
1126 *Geochimica et Cosmochimica Acta*, 48(12), 2659-2668.
- 1127 Summerfield, M.A., 1983a. Petrography and diagenesis of silcrete from the Kalahari Basin  
1128 and Cape coastal zone, Southern Africa. *J. Sediment. Res.* 53, 895–909.
- 1129 Summerfield, M.A., 1983b. Silcrete as a palaeoclimatic indicator: evidence from southern  
1130 Africa. *Palaeogeogr. Palaeoclimatol. Palaeoecol.* 41, 65–79.
- 1131 Torres, M.E., Brumsack, H.J., Bohrmann, G., Emeis, K.C., 1996. Barite fronts in continental  
1132 margin sediments: a new look at barium remobilization in the zone of sulfate reduction  
1133 and formation of heavy barites in diagenetic fronts. *Chem. Geol.* 127, 125–139.

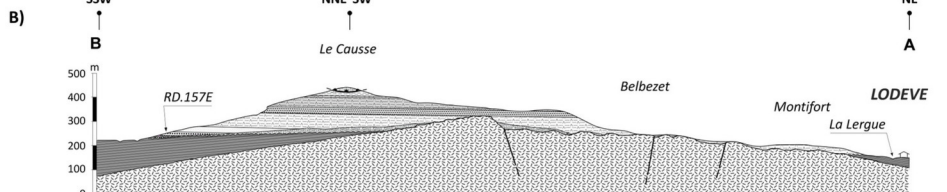
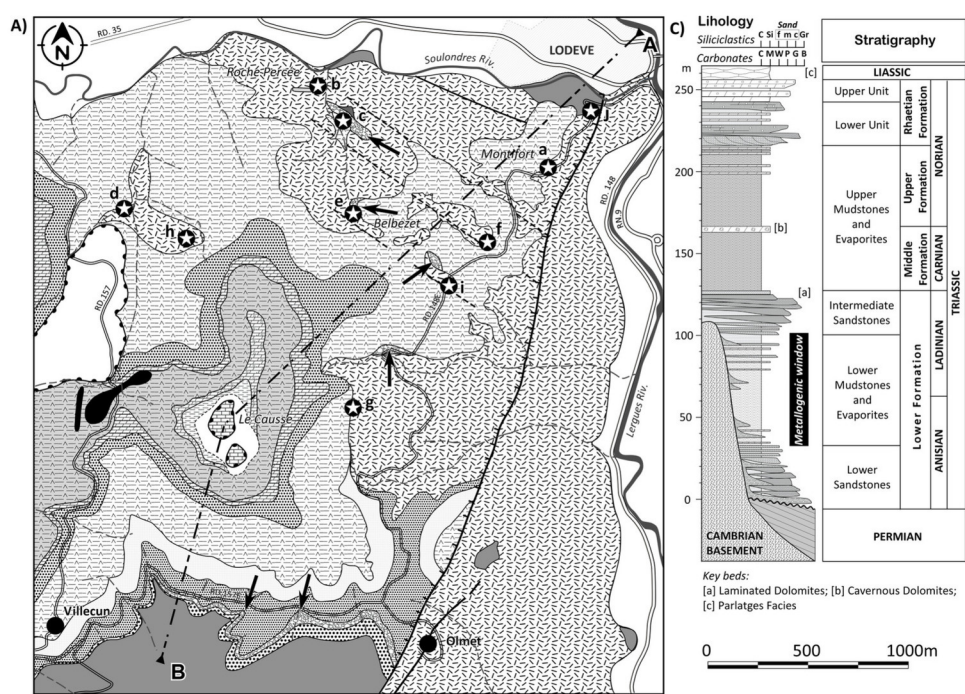
- 1134 Ulliyott, J.S., Nash, D.J., 2016. Distinguishing pedogenic and non-pedogenic silcretes in the  
1135 landscape and geological record. *Proc. Geol. Assoc.* 127, 311–319.
- 1136 Ulrich, M. R., Bodnar, R. J., 1988. Systematics of stretching of fluid inclusions; II, Barite at 1  
1137 atm confining pressure. *Economic Geology*, 83(5), 1037-1046.
- 1138 Van Achterbergh, E., Ryan, C. G., Jackson, S. E., Griffin, W. L., Sylvester, P., 2001. Laser-  
1139 Ablation-ICPMS in the Earth Sciences—Principles and Applications. Mineralogical  
1140 Association of Canada Short Course Series, 40.
- 1141 Wibberley, C.A.J., Petit, J.-P., Rives, T., 2007. The effect of tilting on fault propagation and  
1142 network development in sandstone-shale sequences: a case study from the Lodève Basin,  
1143 southern France. *J. Geol. Soc. London.* 164, 599–608.
- 1144 Wopfner, H., 1983. Environment of silcrete formation: a comparison of examples from  
1145 Australia and the Cologne Embayment, West Germany. *Geol. Soc. London, Spec. Publ.*  
1146 11, 151–158.
- 1147 Wortmann, U.G., Bernasconi, S.M., Böttcher, M.E., 2001. Hypersulfidic deep biosphere  
1148 indicates extreme sulfur isotope fractionation during single-step microbial sulfate  
1149 reduction. *Geology* 29, 647–650.
- 1150 Zhou, X., Chen, D., Dong, S., Zhang, Y., Guo, Z., Wei, H., Yu, H., 2015. Diagenetic barite  
1151 deposits in the Yurtus Formation in Tarim Basin, NW China: Implications for barium  
1152 and sulfur cycling in the earliest Cambrian. *Precambrian Res.* 263, 79–87.  
1153 <https://doi.org/10.1016/j.precamres.2015.03.006>.
- 1154
- 1155





- Plio-Quaternary basaltic volcanism
- Neogene to Quaternary
- Paleogene
- Jurassic
- Triassic
- Middle to Upper Permian
- Lower Permian
- Upper Carboniferous
- Hercynian basement
- Mendic Granite
- Main faults
- ★ Location of the Triassic evaporite samples





### LEGEND

#### Basement

Cambrian dolomites and calcschists

#### Permian deposits

Lower Permian sandstones and pelites

#### Triassic deposits

Lower Sandstones: Basal sandstone body

Lower Sandstones: Debris-flow breccia

Lower Sandstones: Upper sandstone body

Lower Mudstone and Evaporites: Basal sandstone-marls alternations

Lower Mudstone and Evaporites: Marls, gypsum and anhydrite alternations

Intermediate Sandstones

Laminated Dolomites

Upper Mudstones and Evaporites: Marls, gypsum and anhydrite alternations

Upper Mudstones and Evaporites: Cavernous Dolomites

Upper Mudstones and Evaporites: Marls and accessory gypsum and sandstones

#### Jurassic deposits

Hettangian dolomudstones

#### Plio-Quaternary deposits

Alluviums

#### Structures

Main fault

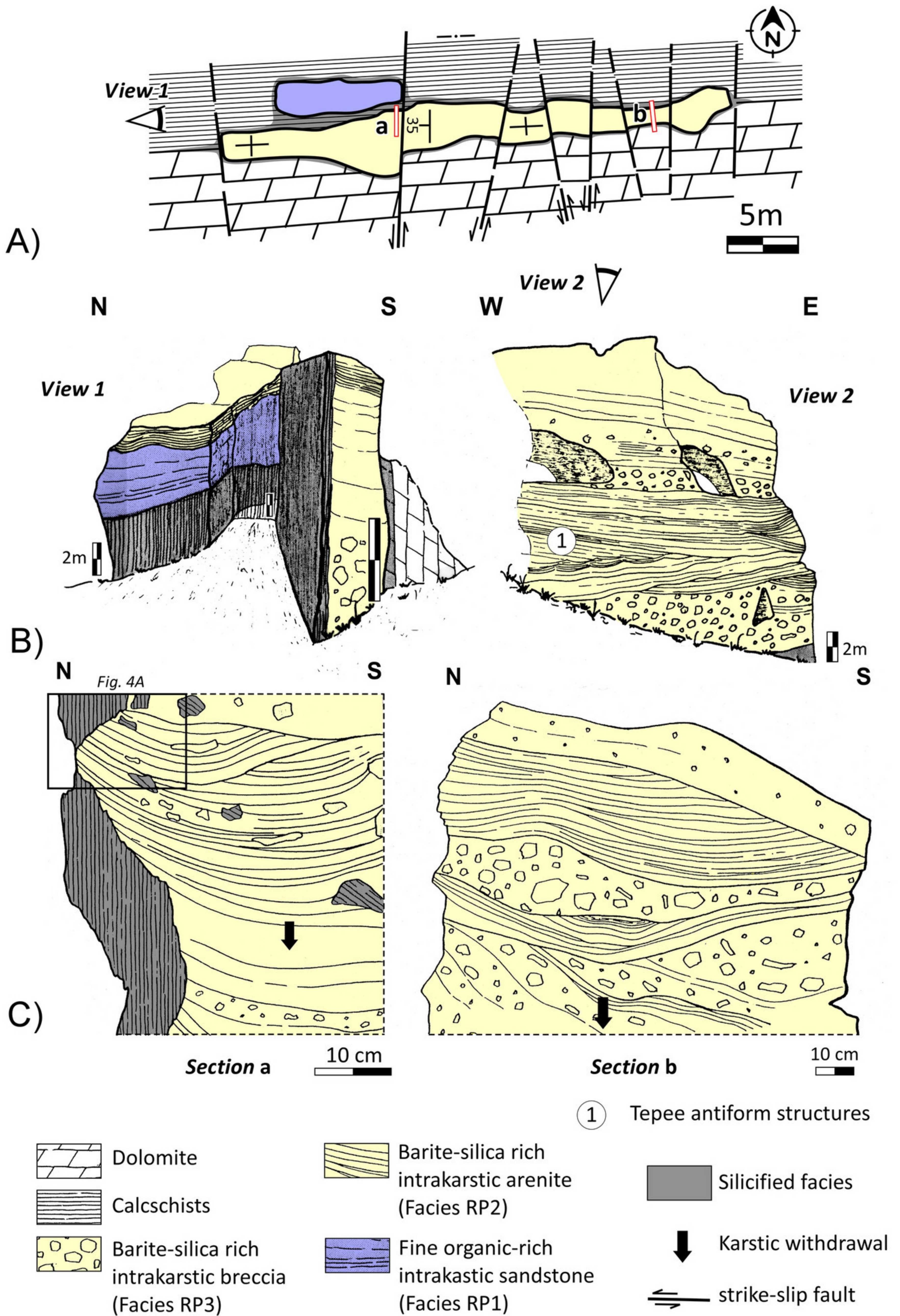
Partly covered fault

Landslide sole

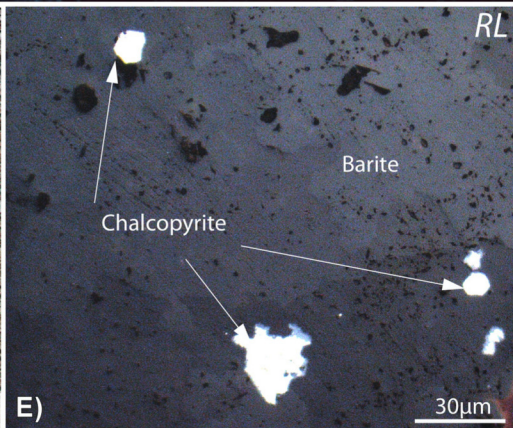
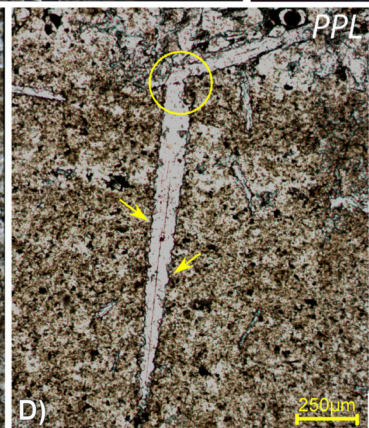
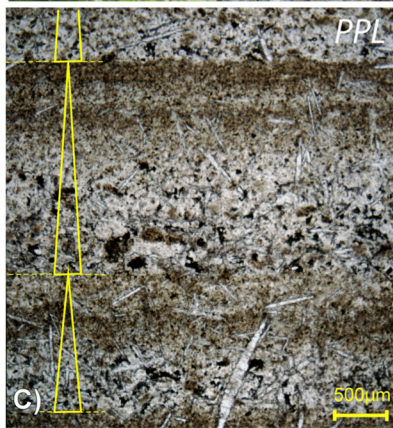
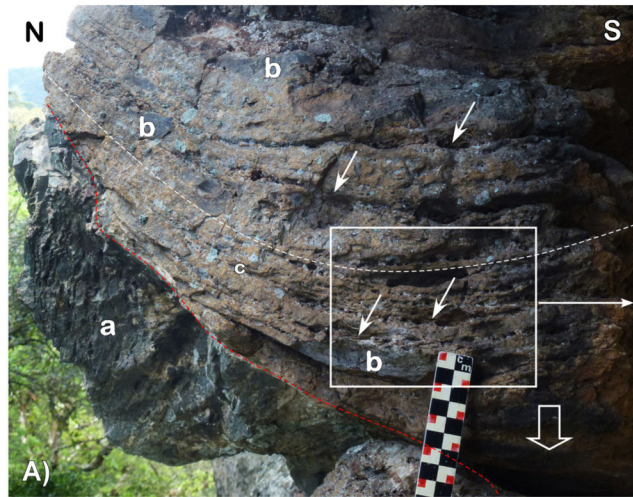
Main transport direction

Studied outcrops





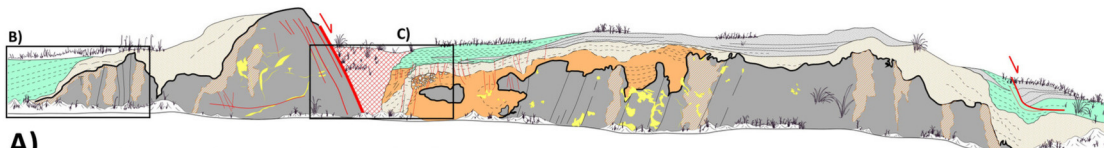







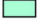
W

E





A)





**Anisian (Lower Mudstone Fm.):**





-  Fine to very fine sandstones
-  Bluish evaporitic marls and thin sandstone interbedded

**Cambrian basement:**

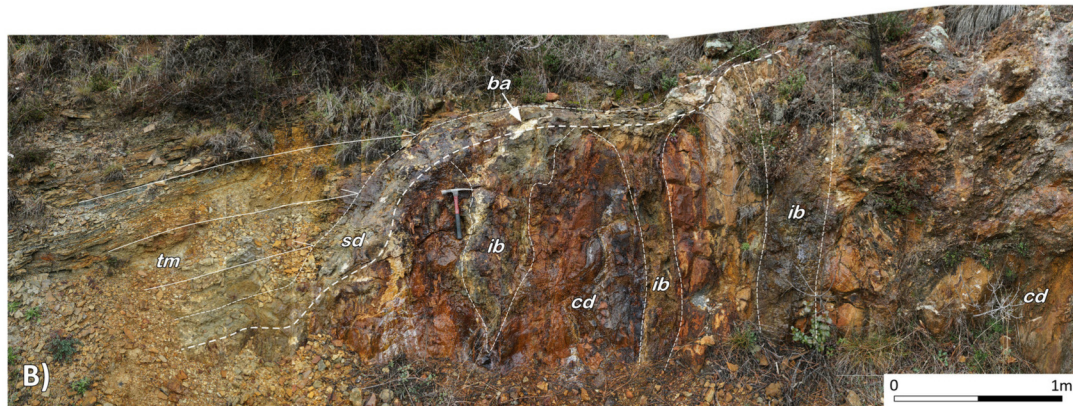
-  Secondary dolomites
-  Karstified paleosurface

**Mineralizations:**

-  Partly oxidized carbonate and sulfides-rich massive to locally bedded very fine sandstone to silstone
-  Partly laminated sulfides-rich bluish vadose silty-claystone (OR)
-  Partly oxidized sulfide-impregnated fracture-controlled bands in the Cambrian dolomites
-  Barite veins and filled cavities in the Cambrian basement

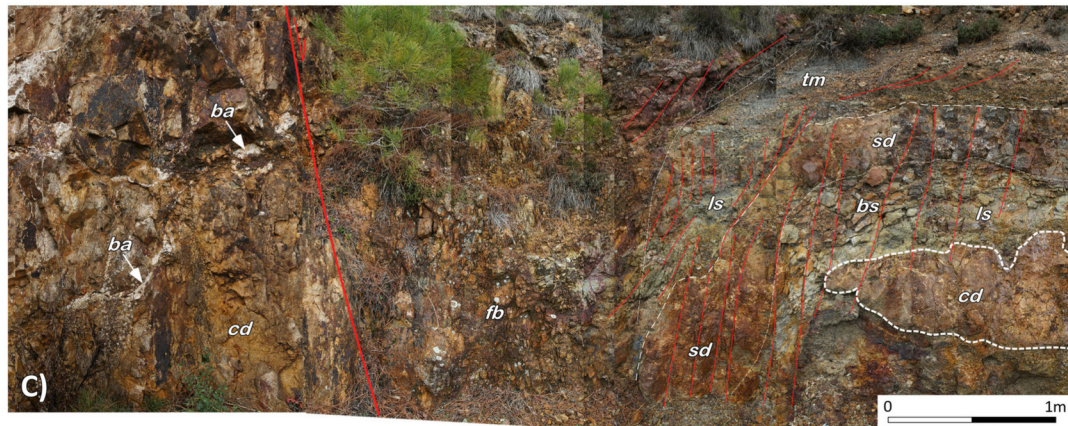
-  Fault breccia
-  Fault
-  Fracture
-  Bedding

0 m 10



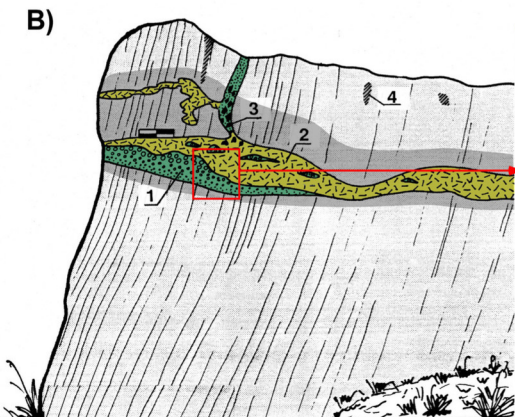
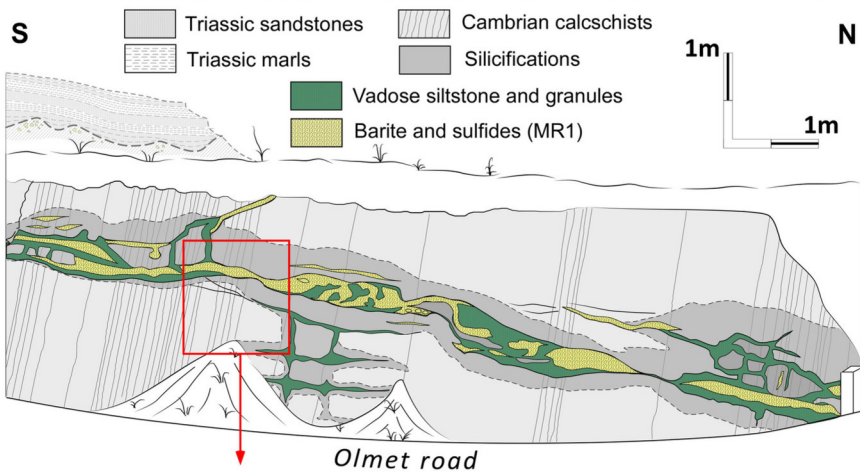
B)

0 1m

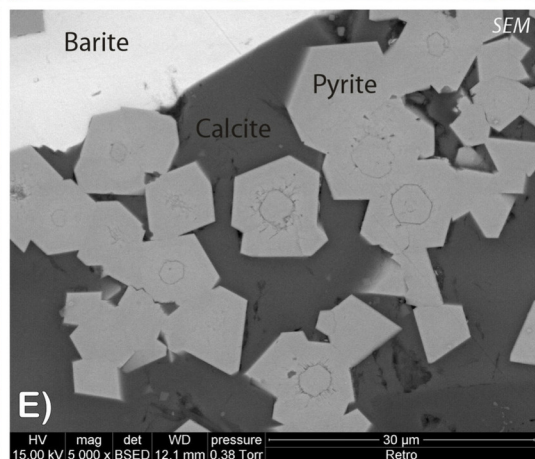
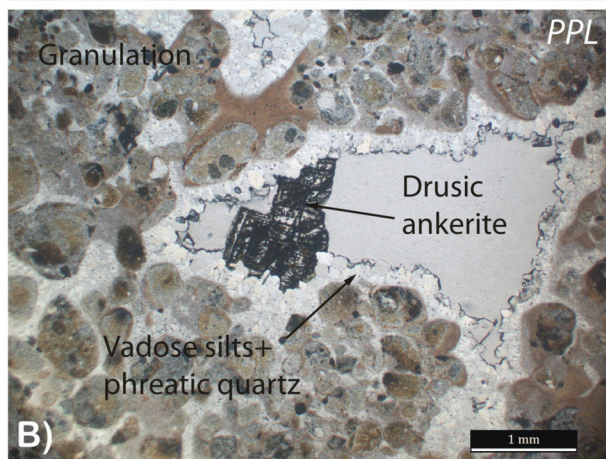
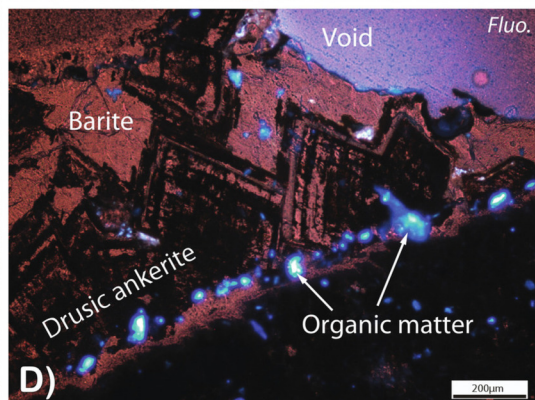
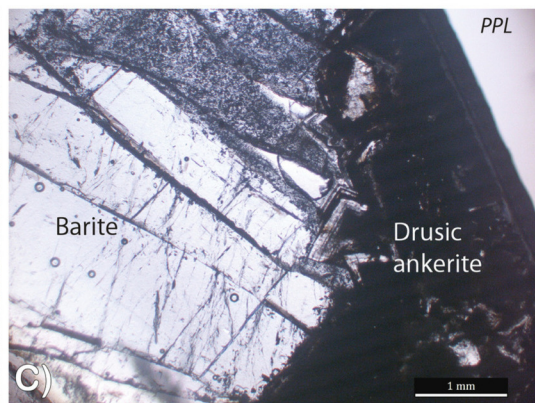
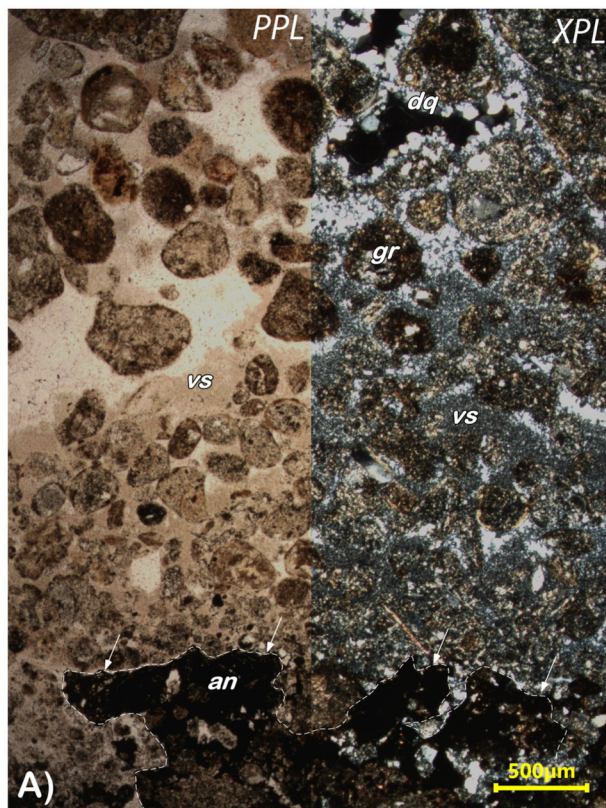


C)

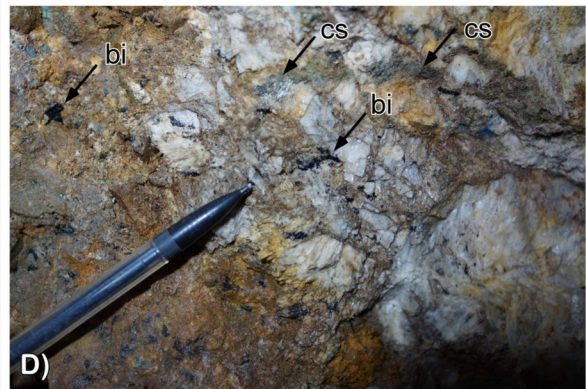
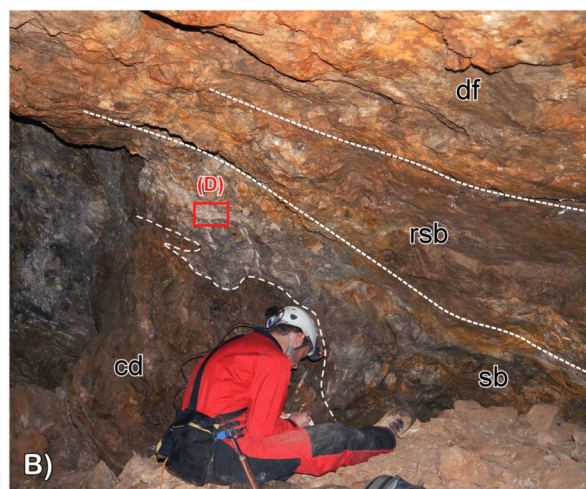
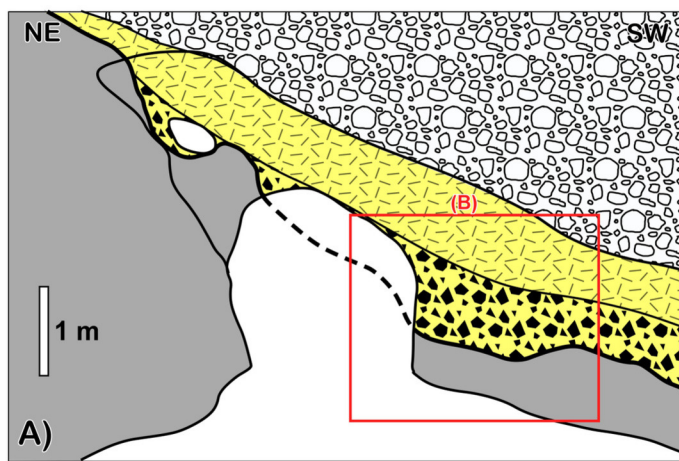
0 1m












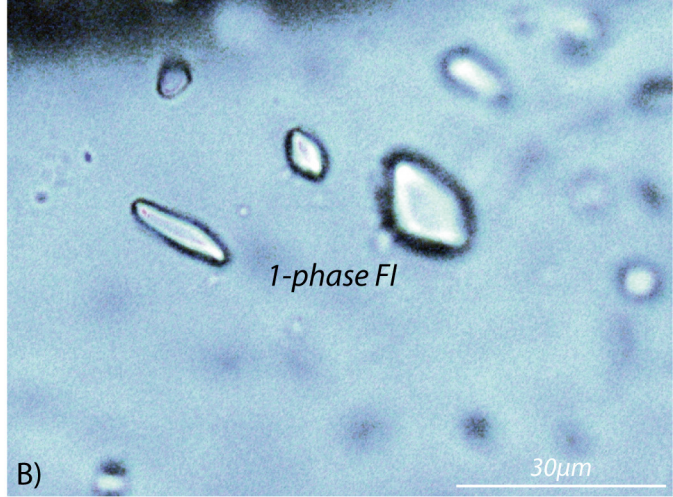
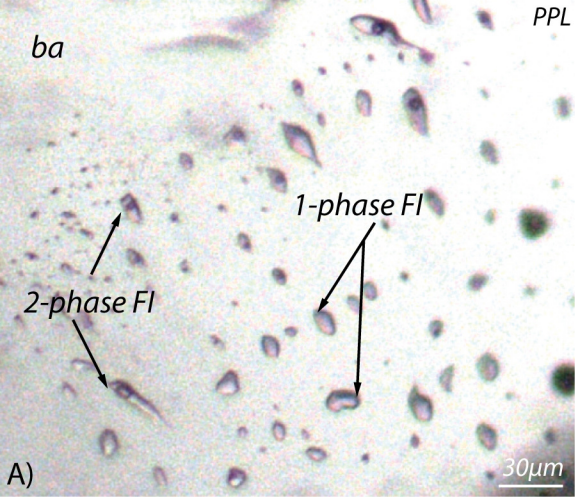


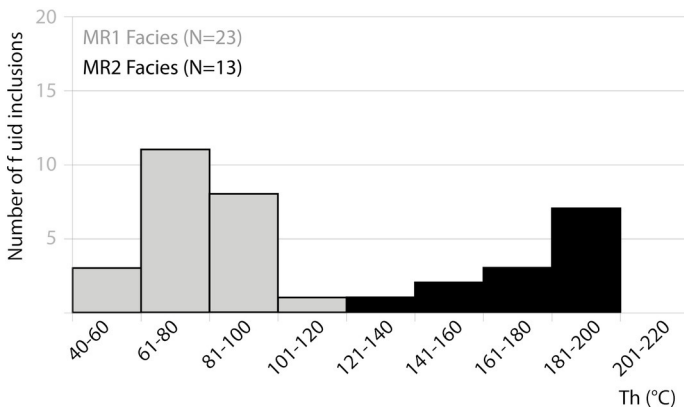
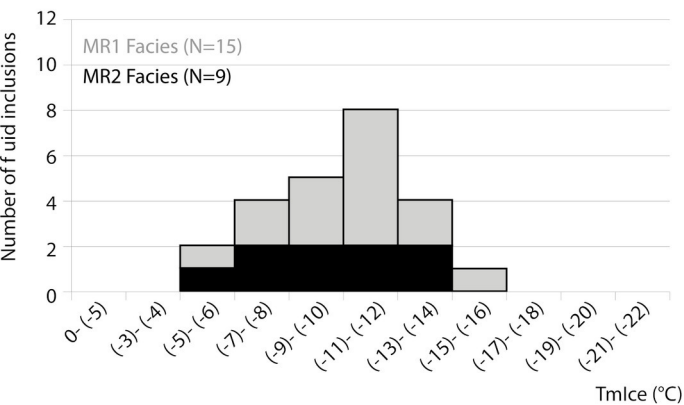
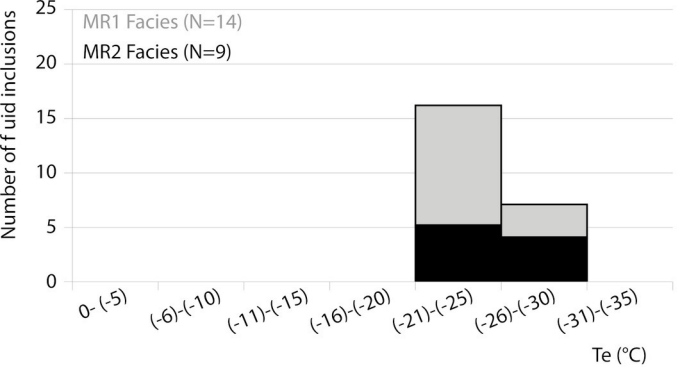
 Matrix supported conglomerate (debris-flow deposit) Middle Triassic

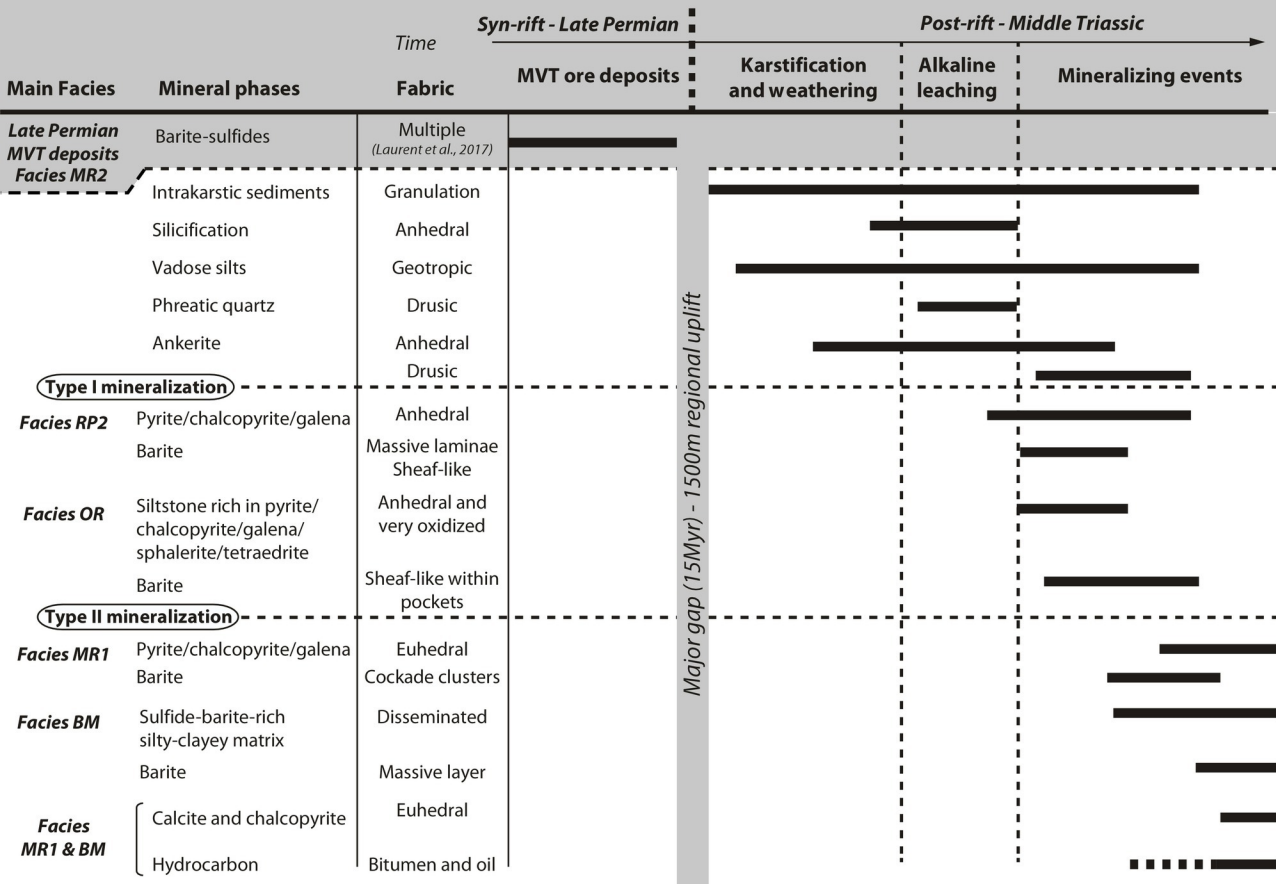
 Reworked bitumen-rich sulfide-barite deposit

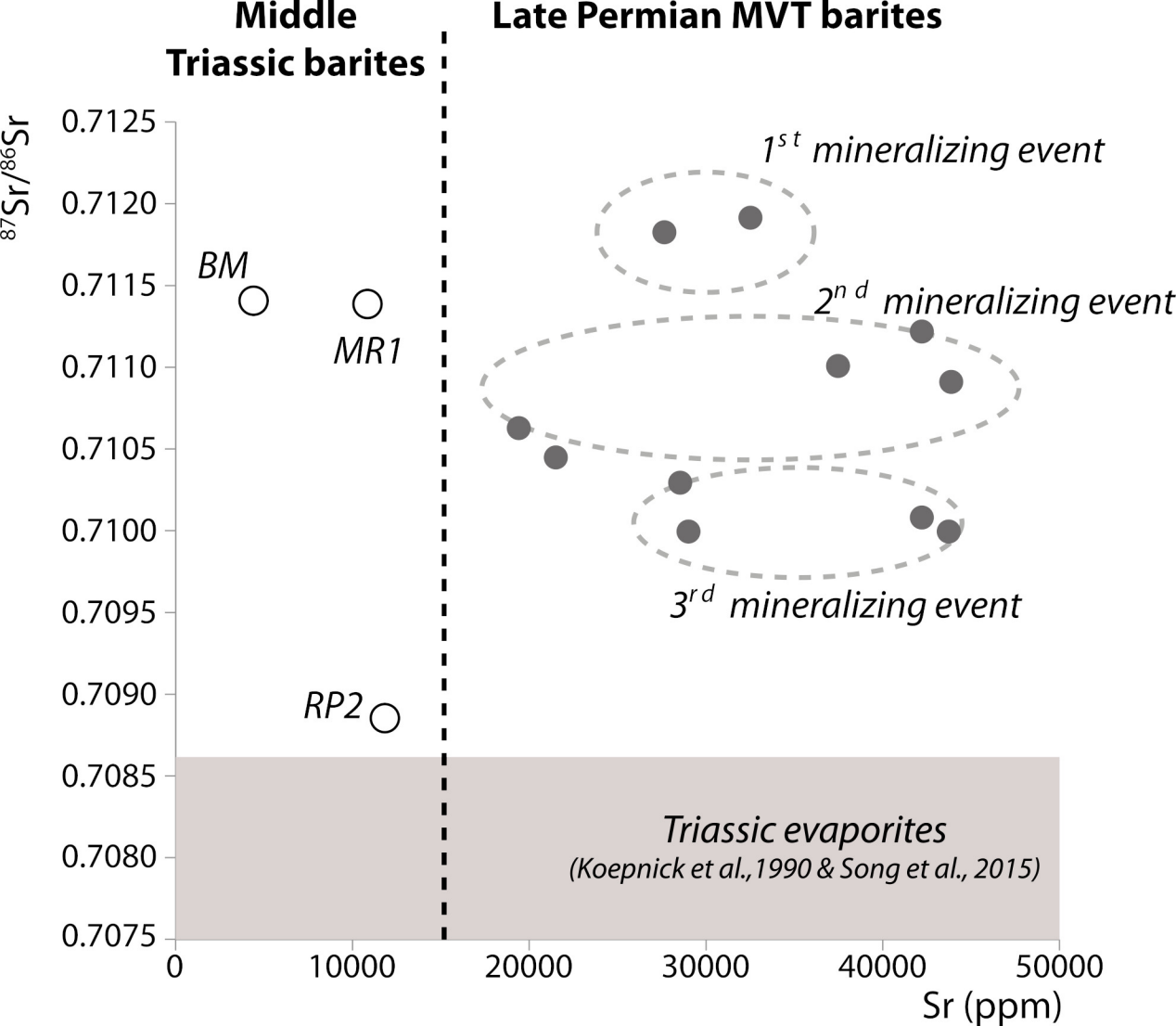
 Partly silicified Cambrian dolomites

 Sulfide-barite-rich silty clayey intrakarstic deposit (**BM**)

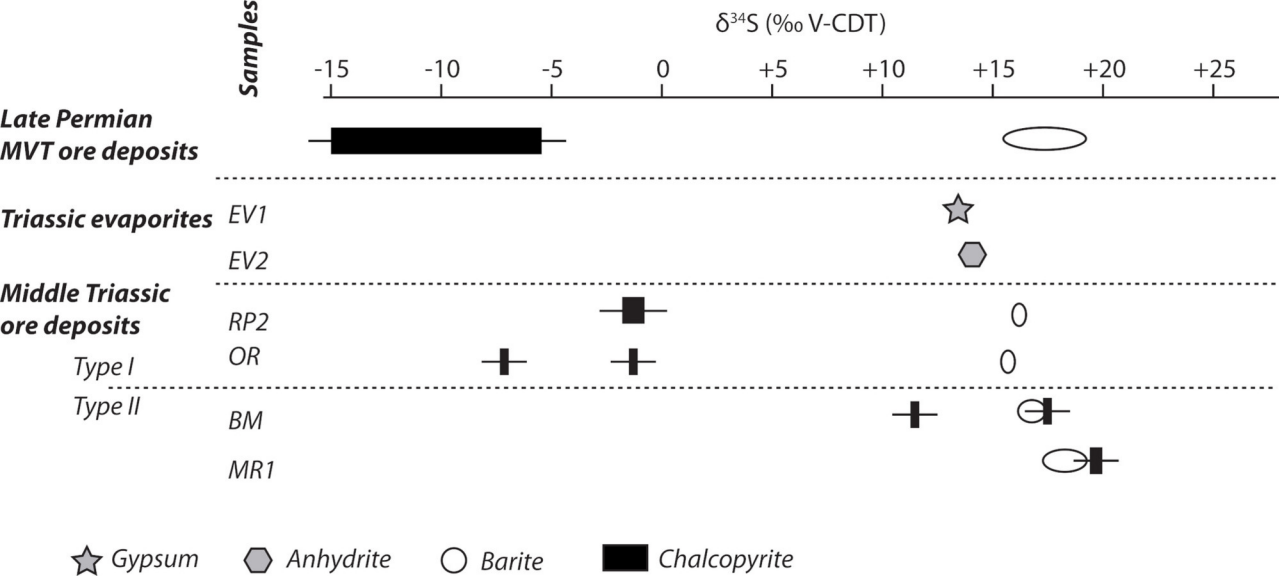


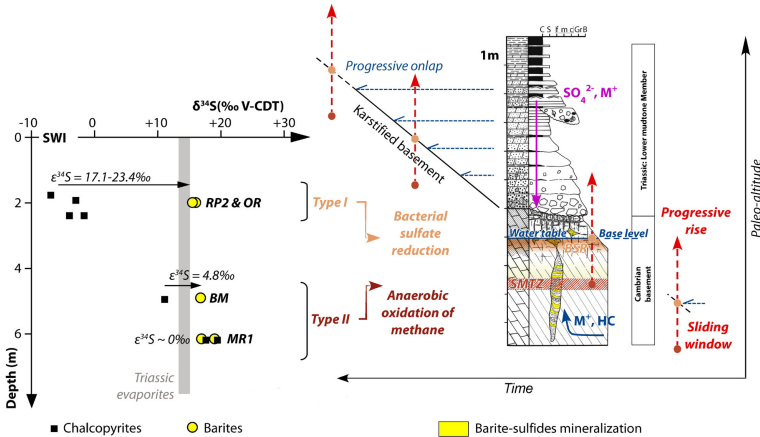




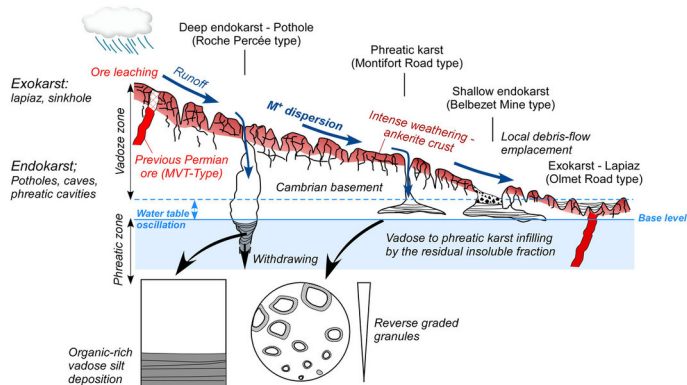






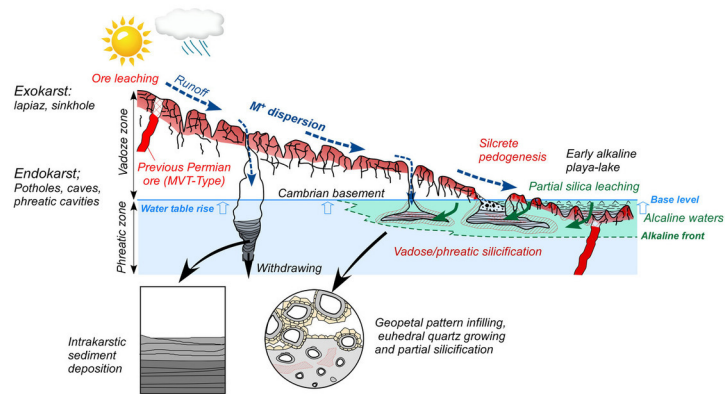


### Stage 1: Intense weathering and epigenic karstification



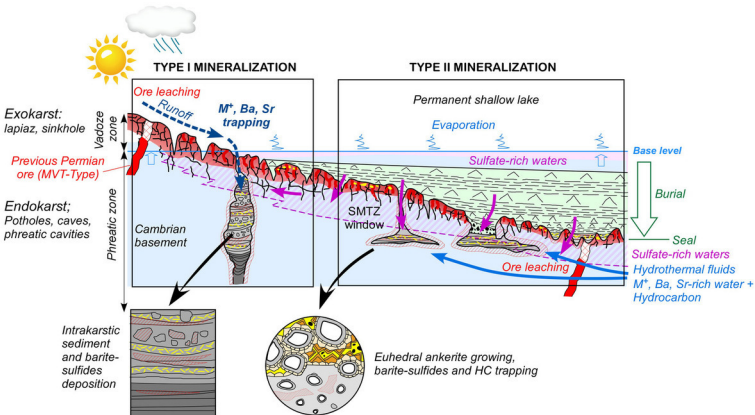
### Stage 2: Initial fringing alkaline playalake

Silica partial leaching and silicifications



### Stage 3: Permanent sulfate-rich shallow-lake - Barite and sulfides trapping

Coeval gravity-driven synsedimentary ore trapping upstream (Type I mineralization) and early burial hydrothermal-driven trapping downstream (Type II mineralization).



<b>Location</b>	<b>Textural facies</b>	<b>Host mineral</b>	<b>Primary fluid inclusion</b>	<b>Te (°C)</b>	<b>TmIce (°C)</b>	<b>Th (°C)</b>	<b>Mean salinity (wt. %eq. NaCl)</b>	
Montifort Road	MR1	Barite (N=23)	Two-phase	-28 to -21	-15 to -5	48 to 102	13.56	
		Barite	Single-phase					
Montifort Road	MR2	Barite (N=13)	Two-phase	-28 to -21	-13 to -5	139 to 195	12.6	
Roche Percée Olmet Road	RP2 OR	Barite	Single-phase					

Location	Textural facies	Host mineral	$^{87}\text{Sr}/^{86}\text{Sr}$	Sr (ppm)	$\delta^{34}\text{S}$ (‰ V-CDT)
<b>Middle Triassic ore deposits</b>					
<b>Roche Percée</b>	RP2	Barite	0.708880	11850.29	+16.2
		Chalcopyrite			-2.1 -1.4
<b>Olmet Road</b>	OR	Barite			+15.7
		Chalcopyrite			-7.2 -1.7
<b>Belbezet Mine</b>	BM	Barite	0.711419	4412.85	+16.2/+16.7
		Chalcopyrite			+11.9 +17.1
<b>Montifort Road</b>	MR1	Barite	0.711386	10739.52	+16.9/+18.5
		Chalcopyrite			+18.9

<b>Triassic evaporites</b>					
<b>Quarry of Notre Dame de Capimont</b>	EV1	Gypsum			+13.7 +14.7
<b>Pégairolles de l'Escalette (drillcore)</b>	EV2	Anhydrite			+14.6 +14.9

<b>Late Permian ore deposits (compilation from Laurent, 2015 and Laurent et al., 2017)</b>					
<b>1<sup>st</sup> mineralizing phase</b>		Barite	0.711913	42192.21	+17.2/+17.6
			0.711826	27764.87	+15.6/+16.9
		Chalcopyrite			-15
<b>2<sup>nd</sup> mineralizing phase</b>		Barite	0.711014	37413.52	+17.3/+17.9
			0.710936	43803.11	+16.6/+16.8
			0.710471	21466.55	+16/+16.4
			0.710637	19500	+17.5
			0.711222	42225.3	+17.8/+18.4
		Chalcopyrite			-10 -13 -6/-5
<b>3<sup>rd</sup> mineralizing phase</b>		Barite	0.710000	43855.8	+16.4/+17.2
			0.710081	32585.4	+16.1/+16.9
			0.710294	28491.79	+16.2/+16.7
			0.710003	28964.38	+17
		Chalcopyrite			-12/-11 -8